Volume 13
Number 1
7 January 2025
Pages 1–502

Journal of Materials Chemistry C

Materials for optical, magnetic and electronic devices

rsc.li/materials-c

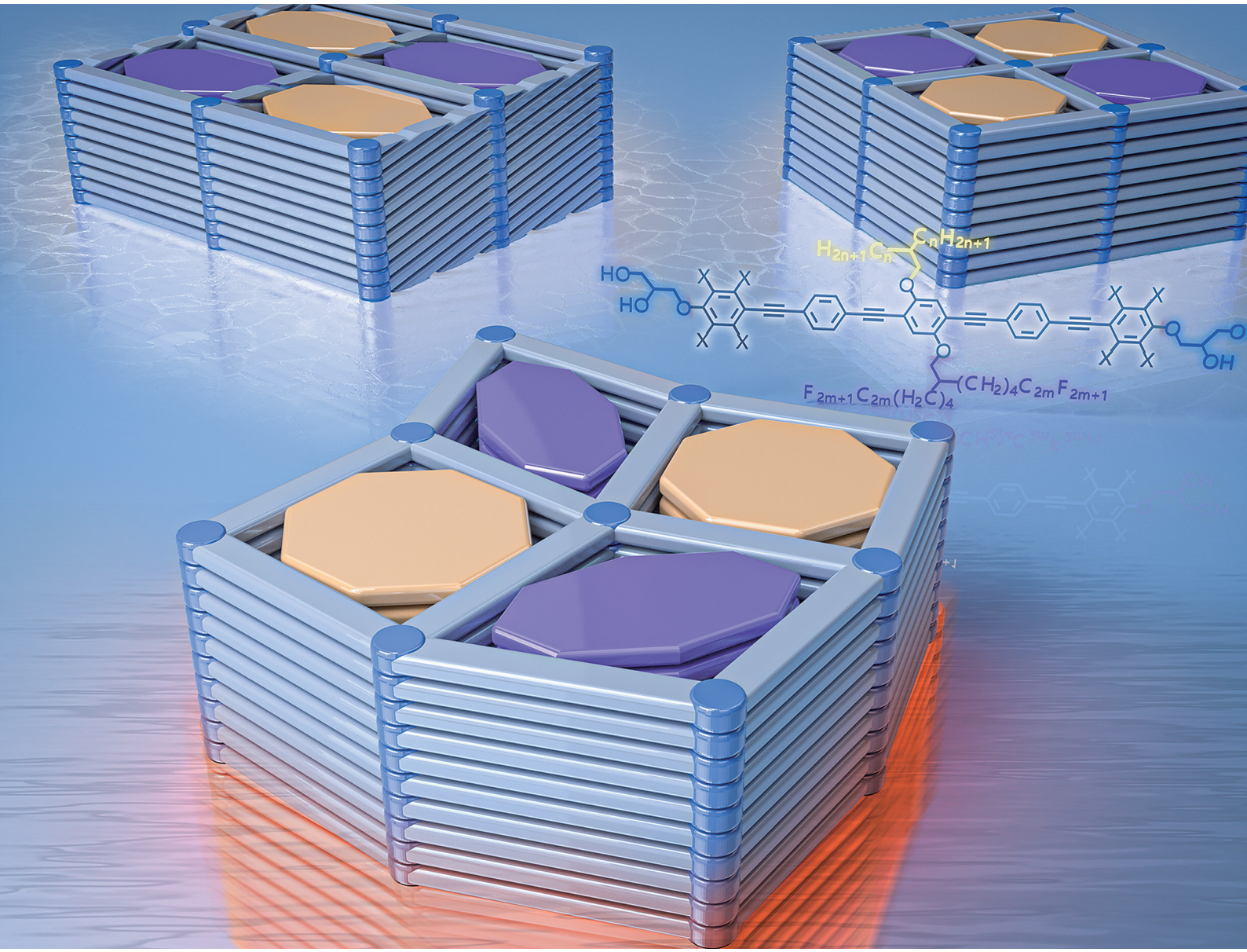

ISSN 2050-7526

ROYAL SOCIETY OF CHEMISTRY

PAPER

Yu Cao, Carsten Tschierske *et al.*

Modifying the liquid crystalline chessboard tiling – soft reticular self-assembly of side-chain fluorinated polyphiles

Journal of Materials Chemistry C

ROYAL SOCIETY OF CHEMISTRY

PAPER

View Article Online
View Journal | View Issue

Cite this: J. Mater. Chem. C, 2025, 13, 37

Modifying the liquid crystalline chessboard tiling – soft reticular self-assembly of side-chain fluorinated polyphiles†

Christian Anders,[a] Virginia-Marie Fischer,[b] Tianyi Tan,[c] Mohamed Alaasar,[a] Rebecca Waldecker,[b] Yubin Ke,[d] Yu Cao,*[c] Feng Liu[c] and Carsten Tschierske*[a]

Development of new functional materials requires the understanding of the fundamental rules of complex superstructure formation in self-assembling systems. Here we report new liquid crystalline honeycombs based on reticular self-assembly of bolapolyphilic rods with two mutually incompatible and branched side-chains, one a semiperfluorinated, the other one a non-fluorinated alkyl chain, all derived from the chessboard tiling by cell deformation due to distinct modes of tilting of π-conjugated rods within or out of the crystallographic plane. Among them the new square + rhomb tiling and a stretched rectangular "chessboard" tiling, both with alternatingly filled prismatic cells, are constructed. Out of plane tilting leads to cell shrinking and cell deformation. Nonfluorinated polyaromatic cores allow a continuously changing tilt, retaining the square cells by simultaneously tilting all molecules, associated with an inversion of the birefringence *via* an optically isotropic state. In contrast, fluorinated cores with different discrete face-to-face stacking modes can assume only discrete tilt angles, which provides rectangular cells with only two walls being tilted. The system offers even more phases including single-color cells with sparingly packed "voids" and a three-color rhomb tiling with additional mixed cells. The research uncovers basic rules of reticular self-assembly by formation of soft multi-functional liquid-crystalline materials.

Received 23rd September 2024,
Accepted 8th November 2024

DOI: 10.1039/d4tc04076g

rsc.li/materials-c

1. Introduction

Liquid crystals (LC) are important advanced materials for application in many fields of modern technology, such as electro-optics, adaptable optics, photonics,[1,2] for biomedical sensing[3] and engineering, for telecommunication devices[4] and in displays for augmented reality[5] to mention only a few.[6–9] Conventional LCs were based on rigid rod-like or disc-like molecules decorated with soft alkyl chains, leading to the classical LC phases such as nematic, smectic and columnar.[6] After recognition of the importance of amphiphilicity and nano-segregation for soft self-assembly[10] attempts were made to create new LC phases and to increase the complexity of LC self-assembly[11,12] towards that required for development of prebiotic structures[13–15] and for novel functions useful in materials science. Early work in this direction was pioneered by H. Ringsdorf, who pointed out the importance of liquid-crystalline self-assembly for structure formation as required in materials science and life science by the unique combination of order with mobility in this state of matter.[16] His group also pioneered the idea of micro-segregation of siloxane-[17] and perfluoroalkyl units[18] as building blocks to modify the properties of LC materials. A part of this work was conducted in collaboration between his group at Mainz University and the LC research groups at Halle University already in the 1980's as an example of east–west collaboration during the Cold-War before the re-unification of Germany[19]. Such farsighted, integrative and charismatic persons like Prof. Ringsdorf would be highly beneficial in today's world.

Inspired by these early contributions of H. Ringsdorf, we developed the concept of polyphilic self-assembly as a tool to organize π-conjugated rods into well-defined complex LC superstructures combining order and mobility. One class of such compounds is provided by the T-shaped, X-shaped, Π-shaped *etc.* molecules based on a simple rod-like unit with sticky hydrogen bonded glycerols at each end and one, two or more flexible side-chains (see for example Fig. 1(a)).[6,20,21] Depending on the rod-length, side-chain number, their length and volume,

[a] Institute of Chemistry, Martin-Luther University Halle-Wittenberg, Kurt-Mothes Str. 2, D-06120 Halle/Saale, Germany
E-mail: Carsten.tschierske@chemie.uni-halle.de
[b] Institute of Mathematics, Martin-Luther University Halle-Wittenberg, Theodor-Lieser-Str. 5, 06120 Halle, Germany
[c] Shannxi International Research Center for Soft Matter, State Key Laboratory for Mechanical Behavior of Materials, Xi'an Jiaotong University, Xi'an 710049, P. R. China. E-mail: yu.cao@xjtu.edu.cn
[d] China Spallation Neutron Source, Institute of High Energy Physics, Chinese Academy of Science, Dongguan 523000, P. R. China

† Electronic supplementary information (ESI) available. See DOI: https://doi.org/10.1039/d4tc04076g

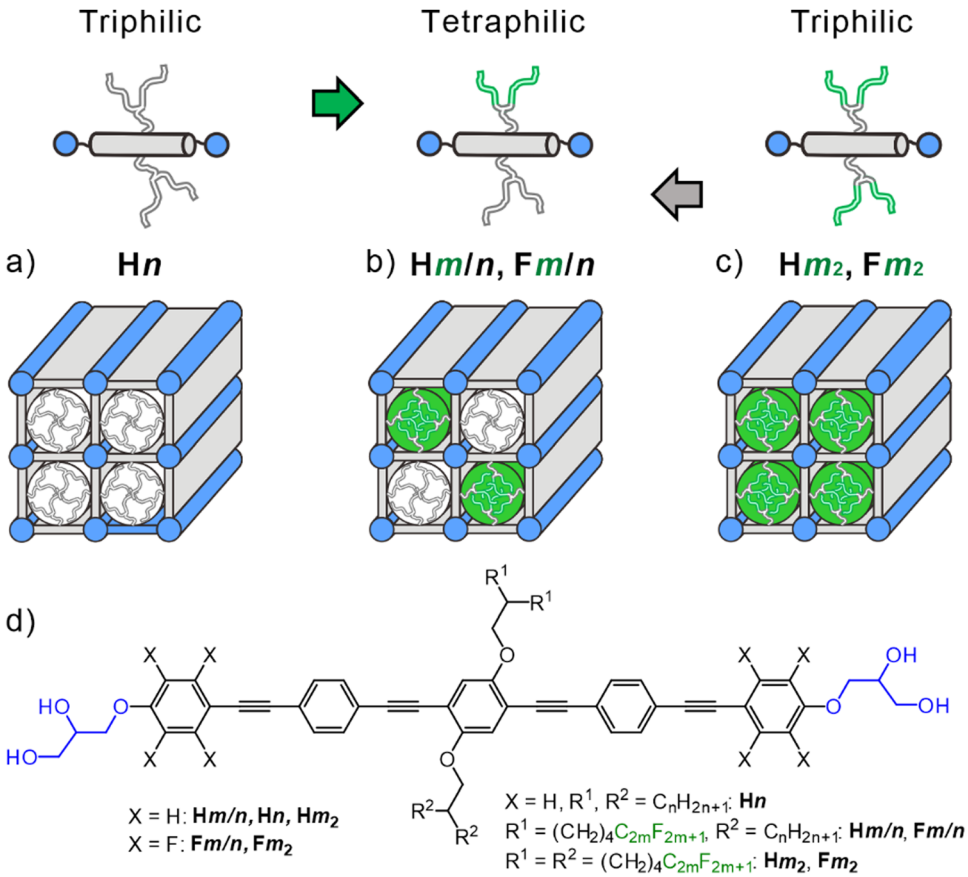

Fig. 1 (a)–(c) Schematics of the bolapolyphiles under discussion and the different types of square honeycomb LC phases; (a) and (c) simple square tilings and (b) chessboard tiling; aromatic cores are in grey, hydrophilic ends are in blue, alkyl side chains are in white and perfluorinated side chains are in green, the cylinders indicate the core shell structure inside the honeycombs cells; (d) shows the structure of the compounds under discussion and used abbreviations; the capital letters **H** and **F** indicate non-fluorinated (OPE) and fluorinated cores (FOPE), respectively; **Hn** stands for the previously reported compounds with two branched alkyl side-chains (R_H with n = length of each branch);[25] compounds **Hm$_2$** and **Fm$_2$** have both side-chains with perfluorinated end groups (R_F chains, m = length of the R_F segment, the aliphatic spacer length is $(CH_2)_4$ in all cases), while compounds **Hm/n** and **Fm/n** combine R_H and R_F chains.

these molecules form LC networks[22,23] and LC honeycomb structures.[24,25] In the honeycombs, the π-conjugated rod-like cores lie perpendicular to the column long axis, held together at the edges by columns formed by the hydrogen bonded glycerol end groups. The resulting prismatic cells are filled by the flexible side-chains.[20,21] Depending on the side-chain volume and the length of the rigid rod-like core, different types of honeycombs were observed, such as triangular, square, pentagonal, and hexagonal, among them also giant honeycombs,[26] superlattices with dodecagonal[27] and octagonal motifs[28,29] and liquid quasicrystalline phases.[30,31] Some of these honeycombs with uniform filling of their prismatic cells have recently also been reproduced by different simulation techniques[32–41] and were found for block copolymers and giant molecules on a larger length scale.[42–47]

Different types of side chains can be used to further increase the structural diversity and complexity of honeycomb LCs by tiling patterns where different chains segregate into distinct prismatic cells, thus leading to so-called multi-color tilings where the cells, arranged in a regular periodic manner, are filled by different materials (Fig. 1(b)); the ''color'' stands for different contents of the prismatic cells.[28,48–56]

Here we report a new class of tetraphilic star-shaped compounds named as **Hm/n**. These newly synthesized compounds are based on a rod-like OPE core[57–61] having glycerol end-groups and different branched chains at opposite sides, one being an alkyl chain (R_H) and the other one with perfluorinated ends (R_F), see Fig. 1(b). As aromatic fluorination is known to have a significant effect on LC self-assembly by introducing polarity[62–64] and modifying the core–core interactions,[65–67] two series of compounds were prepared, one with a non-fluorinated OPE core (**Hm/n**) and a second one with an OPE core having perfluorinated outer benzene rings[61,68] (FOPEs, compounds **Fm/n**, Fig. 1(d)). In addition, the compounds **H8$_2$** and **F8$_2$** with two identical R_F side-chains were synthesized and investigated for comparison purposes.

The new LC phases involve a square + rhomb tiling and a stretched rectangular ''chessboard'' tiling, both with alternating prismatic cells filled by either fluorinated or hydrocarbon chains and a three-color rhomb tiling with additional mixed cells. All structures are derived from the simple chessboard tiling by tilting of the molecular rods, either in the crystallographic plane, or out-of-plane, leading to cell deformation and cell shrinking, respectively. Non-fluorinated polyaromatic rod-like cores allow a continuously changing tilt, retaining the square cells by

simultaneously tilting all molecules, associated with an inversion of the birefringence *via* an optically isotropic state. In contrast, fluorinated cores with different discrete face-to-face stacking modes can assume only discrete tilt angles, which provides rectangular cells with only two walls being tilted. This work provides a guide for bottom-up preparation of complex soft functional arrays of π-conjugated rods at the sub-5 nm scale for use in soft lithography[69] for programmable metafilm[70] and selective absorber.[71] The gained knowledge is also of importance for the construction of new solid-state hydrogen bonded and covalent organic frameworks,[45,72,73] where preparation of multiporous structures combining different cells is still a challenge.[74–76]

2. Results and discussion

2.1 Compound H8$_2$ with two fluorinated side-chains at the non-fluorinated OPE core – emerging tilt, inversion of birefringence and "void" spaces

Compound **H8$_2$** with two identical branched fluorinated chains (Fig. 2(a)) was investigated as reference compound for the evaluation of the specific effects provided by the R_F/R_H combination. The optical texture of **H8$_2$** between crossed polarizers indicate spherulite-like domains with isotropic areas as typical for optical uniaxial columnar LC phases (Fig. 2(c)). Upon cooling there is a strong change of the birefringence as indicated by a color change in the spherulite-like areas, starting around 180 °C. The birefringence (Δn) changes from being negative to $\Delta n = 0$ at 40 °C, at which temperature the texture becomes completely dark (isotropic) and then assumes a deep blue birefringence color after Δn inversion to positive (see Fig. 2(c) and Fig. S8, ESI†). Such a behavior is due to the emergence and growth of a tilt of the rod-like π-conjugated OPE cores in the cylinder walls around the prismatic honeycomb cells, crossing the tilt angle of 35.3° at the Δn inversion point.[27,57] This boundary between negative and positive birefringence is observed if the slow optical axis of the π-conjugated rods assumes the magic angle of 54.7° with respect to the column long axis, *i.e.* 90°–54.7° = 35.3° tilt with respect to the lattice plane.

In the whole LC temperature range on heating and on cooling down to 30 °C the WAXS is diffuse (inset in Fig. 2(e)), as typical for mesophases with no fixed positions of the

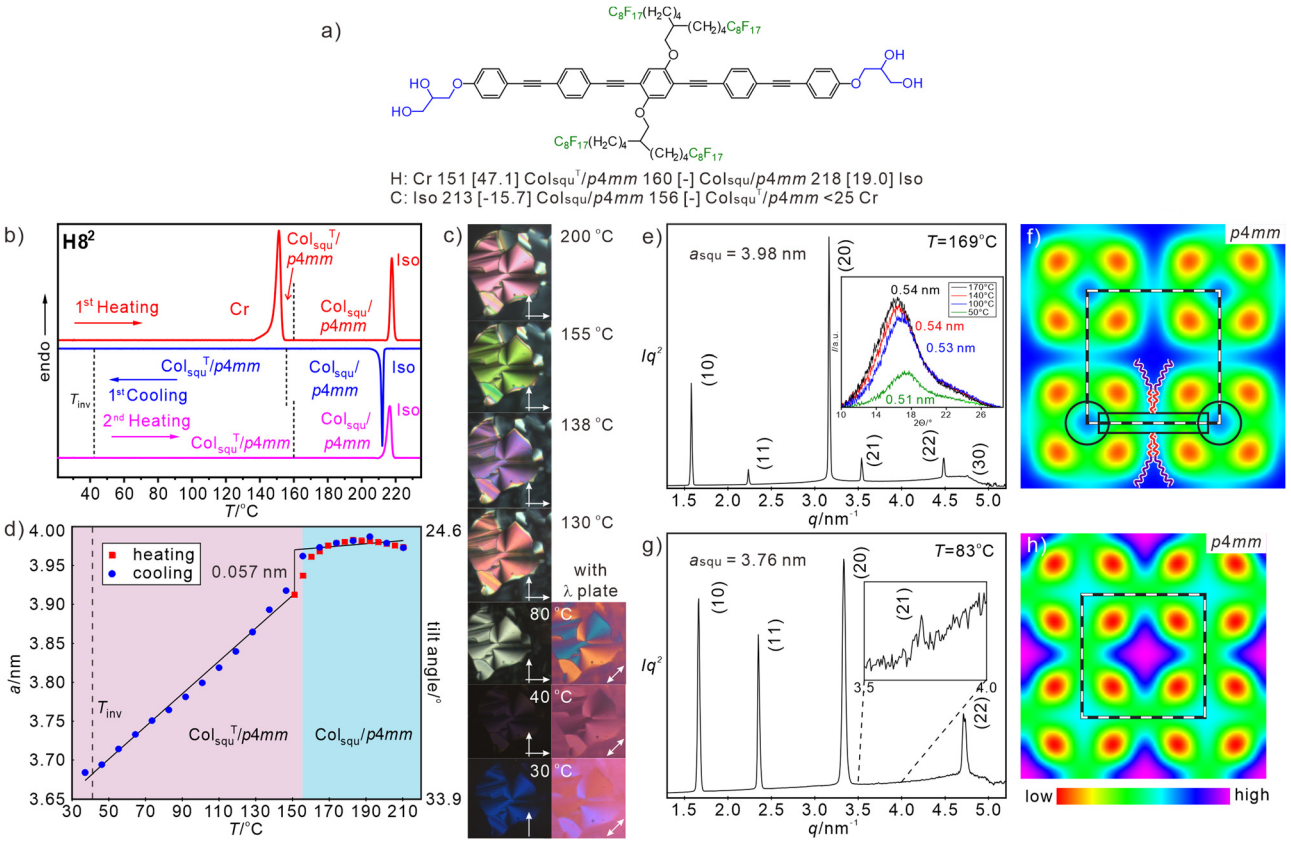

Fig. 2 (a) Formula of **H8$_2$** with transition temperatures (T/°C) and transition enthalpies (ΔH/kJ mol^{-1}), (b) DSC traces, (c) textures as observed between crossed polarizers at the given temperatures, those at the very right are with additional λ-retarder plate, where blue fans in SW–NE direction indicate negative Δn and in NW–SE direction indicate positive Δn, for additional and enlarged textures, see Fig. S8 (ESI†); (d) $a_{squ} = f(T)$ plot, the transition between tilted/non-tilted squares is indicated; (e) and (g) SAXS patterns at the given temperatures (for numerical data, see Tables S10 and S11, ESI†), inset in (e) shows the WAXS (for numerical data, see Table S2, ESI†) and (f), (h) ED maps reconstructed from these patterns (phase choices 000ππ for the first five peaks); lattice is shown by white dashed lines, tiles with molecules along edges are in black dashed lines and in (f) a molecular model is drawn according to the shape and size of **H8$_2$**, black rectangle indicates the aromatic core and the black circles indicate the glycerol nodes.

individual molecules. Together with the fluidity of the compounds this confirms the LC state. The diffuse scattering has a significant tailing towards larger 2θ-values (inset in Fig. 2(e)) and can be separated into a major scattering with maximum at 0.51–0.54 nm, corresponding to the mean distance between the R_F chain segments, and a wider diffuse scattering with a maximum around 0.48 nm (Fig. S10a, c, ESI†). The latter is attributed to the mean distance between the hydrocarbon segments (oligomethylene spacers and polyaromatic OPE cores) and the glycerol of the molecules. The absence of a distinct scattering around 0.36–0.38 nm shows that the OPE cores have a relatively loose packing and can rotate almost freely around their long axes, thus assuming different core–core interaction motifs with different distances, including edge-to-face,[77] face-to-face and other intermediate geometries, separated by relatively small energy barriers.[78]

The SAXS pattern can be indexed to a square lattice with *p4mm* plane group (ratio of *d*-spacings: $1:1/\sqrt{2}:1/2:1/\sqrt{5}:1/\sqrt{8}\ldots$, see Fig. 2(e) and (g)). The lattice parameter at $T = 169$ °C is $a_{squ} = 3.97$ nm which is only slightly smaller than the value typically found for the previously reported R_H substituted compounds **H*n*** ($a_{squ} \sim 4.1$ nm)[25] and is in the range of the molecular length ($L_{mol} = 4.0$–4.4 nm as measured between the ends of the glycerols, depending on the assumed glycerol conformation), thus confirming a square honeycomb with the prismatic cells filled by the side-chains.

Just below the Iso-to-Col_{squ}/*p4mm* phase transition there is a relatively broad orientational order parameter distribution for the OPE rods in the walls, leading to an effective molecular length of about 4.0 nm. In the Col_{squ}/*p4mm* range between 210 and 156 °C there is no significant change of birefringence (Fig. S8a–e, ESI†) and a_{squ} (Fig. 2(d)). Upon cooling to ~190 °C a tiny increase of a_{squ}, indicates an improving order parameter and below ~180 °C a_{squ} starts decreasing. The decrease is small to 156 °C and we attribute it to the development of short-range tilt domains growing in size (Fig. S15, ESI†). At 156 °C there is a small but clearly visible jump to smaller a_{squ}, where the molecules assume a long range correlated tilt with further increasing angle (β) on cooling. This transition to Col_{squ}^{T}/*p4mm* (T stands for tilted) is not associated with a visible DSC peak (Fig. 2(b)) and therefore considered as a weakly first order phase transition, similar to the SmA–SmC transitions in smectic LCs. On further cooling, the lattice parameter decreases almost linearly to a value of $a_{squ} = 3.68$ nm at 37 °C (Fig. 2(d)), corresponding to the temperature of the inversion of birefringence. The calculated tilt of the OPE rods in the honeycomb walls at this temperature is $\beta = 33.2°$ according to $\beta = \cos^{-1}(a_{squ}/L_{mol})$ with $L_{mol} = 4.4$ nm, which is close to the Δn inversion angle of 35.3°.[57] The slight difference is due to uncertainties about the assumed molecular length used for tilt angle calculation, to the uncertainties concerning the orientational order parameter in the walls formed by tilted molecules, and to small contributions of other molecular parts and "form-birefringence" (caused by the columnar structure itself[79]) to the total birefringence. It is noted, that the inversion takes place within the Col_{squ}^{T}/*p4mm* range and is not associated with the $Col_{squ} \rightarrow Col_{squ}^{T}$ transition or any other phase transition. It indicates the temperature of ~35° tilt crossing and the higher this inversion temperature, the larger is the driving force for tilting.

The electron density (ED) map of the Col_{squ}/*p4mm* phase, reconstructed from the SAXS pattern at 169 °C (Fig. 2(e) and (f)) shows a square grid with high ED (blue, purple) which is filled by green medium ED areas with high ED dot (light blue) in the middle, and four low ED dots (yellow/red) in the corners. The light blue dots are assigned to the columns of the glycerols which are interconnected by the OPE rods, while the cells are filled by the high ED areas of the R_F chains together with the medium ED areas resulting from the mixing of R_F segments with the aliphatic spacer units. There is highest ED in the middle of the cells where the R_F chains are concentrated. Somewhat enhanced ED is also found in the middle of the aromatic rods due to the central benzene rings with two electron-rich oxygens. The red low ED dots in the corners of the square honeycomb can only partly be attributed to the low ED aliphatic spacers and mainly to a reduced packing density in the periphery around the R_F cores, because the relatively short and rigid fluorinated chains[52,53] cannot pack sufficiently dense to completely fill the space in the corners of the square cells (see Fig. S18a, ESI†). A related phenomenon was observed in the confined space of micellar aggregates of taper shaped dendritic molecules with relatively rigid peptide based polar groups[80] and in the LC phases of rigid star-shaped molecules.[81] In our case the "voids" are tolerated, because the cohesive energy density of perfluorinated chains is low,[52,53] and hence, the energetic penalty caused by these sparingly packed spaces becomes relatively small. Upon further cooling, the shrinkage of side chains induces a transition to Col_{squ}^{T}/*p4mm* (Fig. 2(g) and (h)). Due to a stronger restriction of the packing of the rigid fluorinated chain segments and the further R_F chain rigidification, the packing problem is retained (compare red dots in the ED maps in Fig. 2(f) and (h)). Such problem provides a driving force for partial chain mixing and core–shell formation in the honeycomb LC phases of compounds **H*m*/*n*** as will be discussed in the following section.

2.2 Compound H8/16 with different side chains at the non-fluorinated OPE core – tilted and non-tilted chessboard tilings

To construct tunable multicolor tilings, applicable as functional materials, one of the semiperfluorinated chains is replaced by a longer alkyl chain of approximately the same volume, generating the **H*m*/*n*** compounds. The transition temperatures and observed mesophases of the three synthesized tetraphilic compounds **H*m*/*n***, together with the corresponding transition enthalpy values and major structural data of the mesophases are collated in Table 1. The LC-Iso transition temperatures, *i.e.* the stability of the LC phases against thermal agitation increases in the order **H16**[25] (141 °C) ≪ **H8/16** (212 °C) < **H8$_2$** (218 °C) by increasing degree of side-chain fluorination. This is mainly due to the stronger incompatibility of the R_F segments with the polyaromatic cores and the glycerol units compared to the aliphatic side chains, and the additional incompatibility between R_F chains and hydrocarbon units (R_H chains and $(CH_2)_4$ spacers), both enhancing the stability

of the self-assembled LC phase.[53,82,83] The relatively small stability increase from **H8/16** to **H8$_2$** is partly due to the reduced contribution of R_F/R_H segregation and the formation of loosely packed "voids" in the $Col_{squ}/p4mm$ phase of **H8$_2$** (see above).

For compound **H8/16** with mixed side-chains of approximately identical side-chain volume at both sides and also similar side-chain volume as **H16**[25] and **H8$_2$**, an optically uniaxial columnar LC phase with spherulite-like texture and large optically isotropic (dark) areas is observed by POM in the whole LC phase range below 202 °C (Fig. S4, ESI†). On cooling, the LC phase is retained down to RT and recrystallization cannot be observed in the second and following heating/cooling DSC scan (Fig. S1d, ESI†), as also found for **H8$_2$**. The SAXS pattern indicates a square lattice (ratio of *d*-spacings: $1:1/\sqrt{2}:1/2:1/\sqrt{5}:1/\sqrt{8},\ldots$) with a lattice parameter of a_{squ} = 5.6 nm at 169 °C (see Fig. 3(a)). The molecular length corresponds approximately to half of the diagonal of the square lattice of $1/2\sqrt{2} \times a_{squ}$ = 4.0 nm. This square lattice can thus be interpreted as a chess-board two-color tiling with alternating fluorine rich and hydrocarbon rich square cells ($Col_{squ}/p4mm^L$, where the superscript "L" indicates the larger superlattice due to two-color tiling), as confirmed by the reconstructed ED map in Fig. 3(b), where purple/blue areas indicate high ED provided by the R_F chains and red/yellow low ED provided by the alkyl chains located in the middles of the alternating square prismatic cells. We note that the decreasing ED in the center of R_F columns (purple → blue) is due to the insufficient length of semifluorinated chain as illustrated by the space filling molecular models in Fig. S18a (ESI†). The square network with medium ED (green color) is formed by the end-to-end connected OPE rods interconnected by the hydrogen bonding networks in the polar columns of the glycerols at the 4-way junctions. Both, the R_F and R_H chain columns are surrounded by uniform medium ED shells (green) without any indication of additional (red) low ED regions. The partial mixing of R_F and R_H chains provides a similar ED as the aromatic cores and the glycerol columns, all together forming a green medium ED continuum. This R_F/R_H chain mixing is obviously required to achieve optimal and uniform space filling in all cells. Especially the space filling around the R_F columns where the alkylene spacers of the semifluorinated side-chains are located is difficult to achieve with exclusively R_F chains. In order to improve space filling, some R_H side chains are required to be incorporated into the aliphatic periphery around the R_F chains and mixed between the aliphatic spacer units, thus removing any loosely packed areas (Fig. S18c, ESI†). Because R_H and R_F chains are fixed to opposite sides of the OPE cores, this partial mixing of the R_H chains into the R_F cells requires the mixing of their R_F chains at the opposite side into the adjacent R_H-filled cells. Thus, also a mixed R_F/R_H shell develops around the R_H cores.

Table 1 LC phases, transition temperatures, associated enthalpy values, lattice parameters and major structural data of compounds **H*m/n*** and **F*m/n***[a]

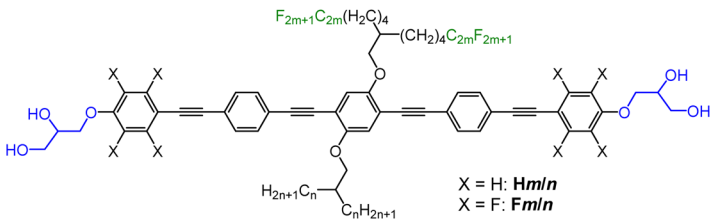

H*m/n*	Phase sequence *T*/°C [Δ*H* kJ mol^{-1}]	T_{inv}/°C	*a*, *b*/nm (*T*/°C)	n_{wall}	L_{wall}
H8/16	H: Cr 96 [48.5] $Col_{squ}^{T}/p4mm^{L}$ 160 [−] $Col_{squ}/p4mm^{L}$ 212 [24.9] Iso	73	5.55 (169)	1.2	3.92
	C: Iso 202 [−20.2] $Col_{squ}/p4mm^{L}$ 160 [−] $Col_{squ}^{T}/p4mm^{L}$ < 20 Cr		5.02 (46)	1.0	3.55
H8/14	H: Cr 104 [47.1] $Col_{squ}^{T}/p4mm^{L}$ 162 [1.2] $Col_{squ}/p4mm^{L}$ 200 [18.3] Iso	105	5.57 (183)	1.3	3.94
	C: Iso 197 [−18.7] $Col_{squ}/p4mm^{L}$ 161 [−0.8] $Col_{rec}^{T}/p2mm^{L}$ 119 [−] $Col_{squ}^{T}/p4mm^{L}$ < 20 Cr		10.41; 5.20 (119)	1.1	3.67
			4.99 (74)	1.0	3.53
H7/14	H: Cr < 20 $Col_{squ}^{T}/p4mm^{L}$ 151 [2.3] $Col_{squ}/p4gm$ 194 [16.4] Iso	118	8.08 (169)	1.37	4.27
	C: Iso 188 [−14.7] $Col_{squ}/p4gm$ 137 [−3.9] $Col_{squ}^{T}/p4mm^{L}$ < 20 Cr		8.21 (142)	1.42	4.34
			4.96 (101)	1.0	3.51
F8/16	H: Cr 78 [53.6] $Col_{rec}^{T/2}/c2mm$ 193 [4.0] $Col_{squ}/p4mm^{L}$ 197 [29.5] Iso	—	5.61 (192)	1.2	3.97
	C: Iso 193 [−34.8] $Col_{squ}/p4mm^{L}$ 191[b] $Col_{rec}^{T/2}/c2mm$ 26 [−24.0] Cr		8.32, 6.77 (146)	1.1	4.16/3.38
F8/14	H: Cr 81 [49.4] $Col_{rec}^{T/2}/c2mm$ 191 [4.4] $Col_{squ}/p4gm + p4mm^{L}$ 195 [26.7] Iso	—	5.54 (189)	1.2	3.92
	C: Iso 192 [−27.4] $Col_{squ}/p4gm + p4mm^{L}$ 189 [−4.4] $Col_{rec}^{T/2}/c2mm$ 25 [−17.7] Cr		8.09 (189)	1.3	4.29
			8.17, 6.43 (156)	1.1	4.09/3.21
			7.86, 6.22 (74)	1.0	3.93/3.11
F7/14	H: Cr 35 [21.5] $Col_{rec}^{T/2}/c2mm$ 183 $Col_{squ}/p4gm$ + M1 186 [27.8][b] Iso	—	8.20 (178)	1.4	4.33
	C: Iso 182 [−22.6] $Col_{squ}/p4gm$ + M1 177 [−5.0][c] $Col_{rec}^{T/2}/c2mm$ 24 [−21.5] Cr		8.10, 6.02 (156)	1.0	4.06/3.01

[a] Transition enthalpies and peak temperatures from 1st DSC heating (H)/cooling (C) scans at 10 K min^{-1} (see Fig. 4(a) and Fig. S1a and d, ESI for DSC traces); abbreviations: n_{wall} = average number of molecules in the lateral cross section of the honeycomb walls with a height of 0.45 nm; L_{wall} = distance between the centers of the polar glycerol columns along the honeycomb walls; Cr = crystalline solid; $Col_{squ}^{T}/p4mm^{L}$, $Col_{squ}/p4mm^{L}$ = two color chessboard tiling; superscript ^{L} indicates a large lattice due to the multicolor tiling; superscript ^{T} indicates a tilted organization in the honeycomb walls; $Col_{squ}/p4gm$ = two color square-rhomb tiling; $Col_{rec}^{T}/p2mm^{L}$ = 3-color tiling by slightly rhombic cells, see Fig. 4(d); $Col_{rec}^{T/2}/c2mm$ = two color tiling by rectangular cells, formed by a combination of tilted and non-tilted walls; M1 = unknown birefringent mesophase; Iso = isotropic liquid; SAXS data were recorded in cooling scans; for more structural data, see Table S22 (ESI). [b] Transitions are not resolved, the enthalpy value includes both transitions. [c] The transition M1 to $Col_{rec}^{T/2}/c2mm$ is slow and takes place betweem 177 and 140 °C, see Fig. S5c–f.

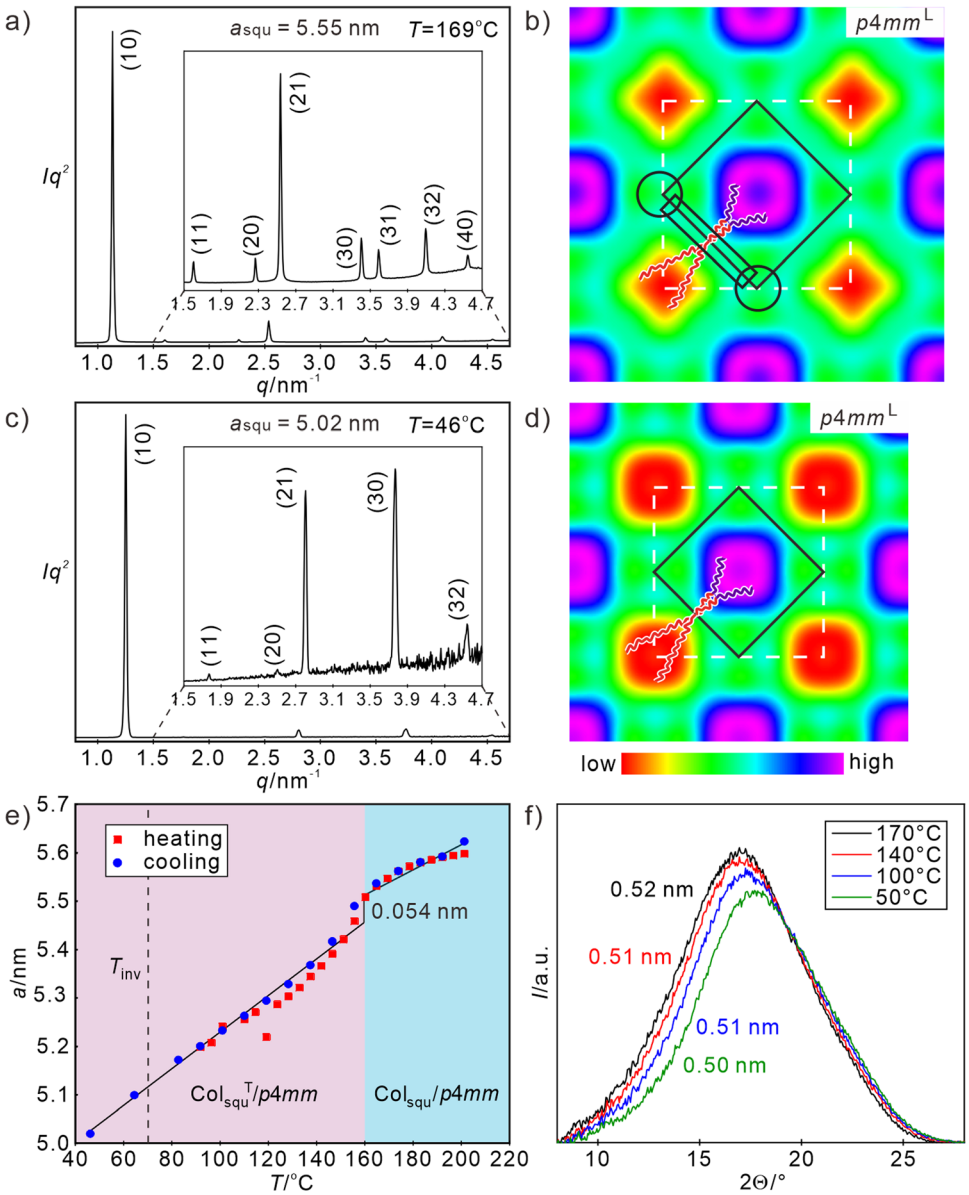

Fig. 3 (a) and (c) SAXS patterns (for numerical data, see Tables S8 and S9, ESI†) and (b) and (d) reconstructed ED maps of the Col$_{squ}$/*p4mm*^{L} phase of **H8/16** at 169 °C and 46 °C, respectively (phase choices 00π0πππ and 00π0ππ); white dashed lines indicate the unit cell and solid black lines the shape of one honeycomb cell, in (b) a molecular model is drawn, black rectangle indicates the aromatic core and the black circles indicate the glycerol nodes; (e) shows the temperature dependence of a_{squ}; (f) shows the diffuse WAXS scatterings at different temperatures (for numerical WAXS data, see Table S1, ESI†). For DSC data and textures, see Fig. S1d and S4 (ESI†).

The mixing allows optimized space filling in both types of cells and increases the entropy, both stabilizing the chess board tiling. However, chain mixing also creates additional interfaces, leading to a kind of core–shell structure of the prismatic cells in the honeycombs. Hence, the chessboard has differently colored cores surrounded by mixed shells.

The diffuse WAXS pattern, confirming the LC state has its maximum around 0.50–0.52 nm (Fig. 3(f)), being slightly shifted to shorter distances compared to **H8$_2$**, in line with a partial R_F/R_H chain mixing. The presence of the alkyl chains changes the shape of the WAXS scattering a bit, showing a smoother declination towards larger 2θ values (shorter distances). The absence of any shoulder or additional scattering at larger 2θ-values corresponding to a distance around 0.36–0.38 nm again indicates the absence of a close face-to-face stacking (see also Fig. S9a–c, ESI†). Notably, the chessboard tiling is directly formed from the isotropic liquid state without passing any region with a simple (color-mixed or only short-range segregated) square honeycomb, as previously reported for all other multi-color square tilings.[49,51] The side-by-side organization of R_F segments in the branched chains obviously provides a cooperativity, supporting the R_F/R_H segregation.

The lattice parameter a_{squ} of the square honeycomb of **H8/16** decreases from 5.6 nm at 201 °C to 5.0 nm at 46 °C,

corresponding to a reduction of the honeycomb wall length from L_{wall} = 3.98 to 3.55 nm (Fig. 3(e)) and development of a 36.2° tilt, very similar to **H8$_2$**. The discontinuity in the $a_{squ} = f(T)$ diagram in Fig. 3(e) indicates the onset of uniform tilt around 160 °C, *i.e.* close to the temperature observed for **H8$_2$**. Again, this transition is not associated with any transition enthalpy (see DSC traces in Fig. S1d, ESI†), in line with the almost continuous and reversible character of this Col$_{squ}$/*p4mm*^{L}–Col$_{squ}$^{T}/*p4mm*^{L} transition (see Fig. 3(e)). Also similar to **H8$_2$**, there is an inversion of Δn in the Col$_{squ}$^{T}/*p4mm*^{L} range around 73 °C (Fig. S3, ESI†). The enhanced inversion temperature and the larger tilt angle at 45 °C indicate a slightly stronger tilt of the OPE cores in the case of compound **H8/16**, which is assumed to be (at least partly) due to the chain mixing in the periphery around the R_F chains which avoids the sparingly packed areas in the corners of the squares (Fig. 3(b)); thus, an overall denser packing is achieved.

2.3 Reduction of R_H side chain length – three-color tiling

For compound **H8/14** with a shorter alkyl side chain the same sequence Col$_{squ}$^{T}/*p4mm*^{L}–Col$_{squ}$/*p4mm*^{L}, as found for **H8/16**, is observed with a transition between them at 162 °C on heating, in this case associated with a DSC endotherm (1.2 kJ mol^{-1}, see Fig. 4(a)). Though the lattice parameters are similar (a_{squ} = 5.6 nm at 183 °C in Col$_{squ}$/*p4mm*^{L} and a_{squ} = 5.0 nm at 74 °C in Col$_{squ}$^{T}/*p4mm*^{L}, for SAXS patterns and ED maps, see Tables S5–S7 and Fig. S11a, b, S12, ESI†) if compared with **H8/16** (Fig. 3(e)), this first order transition is associated with a much larger jump of the cell size (Fig. 4(b)), and hence, tilt angle. Such stronger tilt, also indicated by the increasing birefringence inversion temperature from 73 to 105 °C (Fig. S3, ESI†) originates from side-chain volume reduction.

While a direct transition from Col$_{squ}$^{T}/*p4mm*^{L} to Col$_{squ}$/*p4mm*^{L} is observed on heating compound **H8/14**, on cooling the reverse transition from Col$_{squ}$/*p4mm*^{L} to Col$_{squ}$^{T}/*p4mm*^{L} is associated with the formation of an intermediate biaxial columnar phase between 161 and 119 °C (Fig. 4 and Fig. S3, ESI†). In the DSC cooling traces there is a relatively broad peak at 150–160 °C, while the second transition to the uniaxial Col$_{squ}$^{T}/*p4mm*^{L} phase is not observed, probably, because the transition is too slow. The SAXS pattern of this biaxial LC phase is indexed to a rectangular lattice with *p2mm* plane group and parameters a_{rec} = 10.4 and b_{rec} = 5.26 nm (Fig. 4(c)), where b_{rec} is only slightly smaller than a_{squ} in the adjacent Col$_{squ}$/*p4mm*^{L} phase and a_{rec} being almost twice as large as b_{rec}. This means that the number of tiles per unit cell increases from only two in the

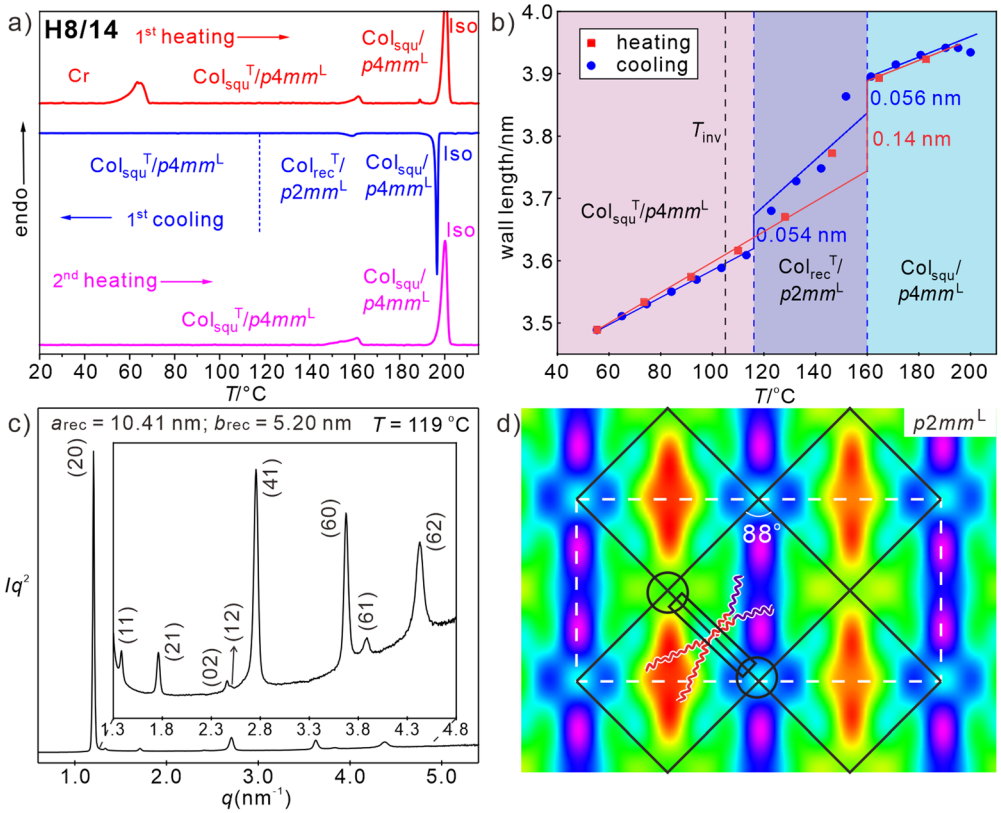

Fig. 4 Compound **H8/14**: (a) DSC traces, (b) wall length depending on temperature diagram on heating (red) and on cooling (blue); the dashed blue lines indicate the Col$_{rec}$^{T}/*p2mm*^{L} range on cooling, T_{inv} is the birefringence inversion temperature; (c) SAXS pattern and (d) reconstructed ED map of the Col$_{rec}$^{T}/*p2mm*^{L} phase at 119 °C (ππππππ00, except for (12)) with the lattice shown by white dashed lines and the tiles with molecules along the edges shown as black solid lines; overlaid is a sketch of the organization of the molecules, black rectangle indicates the aromatic core and the black circles indicate the glycerol nodes; SAXS data and ED maps of the square phases, see Tables S5–S7, Fig. S11a,b and S12 (ESI†), for WAXS data, see Fig. S9b and Table S1 (ESI†) and for POM textures Fig. S3 (ESI†).

chessboard phase ($p4mm^L$) to four in $Col_{rec}{}^T/p2mm^L$. The ED map in Fig. 4(d) shows three different types of almost square cells. Those with high ED are mainly filled with the R_F chains and the other two with low ED cores are mainly filled by the alkyl chains. There is a slight difference in ED between the two types of low ED cells, indicating a different degree of mixing of the R_F chains into the R_H domains, thus leading to a three-color tiling. The formation of this intermediate phase upon cooling is associated with a reduction of L_{wall} from 3.9 to 3.7 nm *i.e.* with the onset of a tilt of 33°, which is a bit smaller than found at the same temperature in the $Col_{squ}{}^T/p4mm^L$ phase (L_{wall} = 3.6 nm, β = 35°) on heating (see Fig. 4(b)). This onset of uniform tilt leads to a decreasing birefringence of the spherulite-like texture which further decreases at the transition to the low temperature $Col_{squ}{}^T/p4mm^L$ phase (see Fig. S3, ESI†). The ED map in Fig. 4(d) indicates a preferred organization of the R_F and R_H chains along one of the square diagonals, reducing the symmetry and leading to a slight rhombic deformation of the almost square cells (rhombic angle of 88°).

It appears that there are two options for the developing tilt, occurring either out of the crystallographic *a–b* plane, in this way shrinking all square sides simultaneously and retaining the square cells as found in the $Col_{squ}{}^T/p4mm^L$ phase, or tilt within the crystallographic plane, leading to a reduction of the cell size by deformation of the squares to rhombs (see Fig. 8(b) in Section 4). In the present case both tendencies compete with each other in a certain temperature range. On heating exclusive the out-of-plane tilt is found with a direct $Col_{squ}{}^T/p4mm^L$ to $Col_{squ}/p4mm^L$ transition, while on cooling the reduced side-chain volume of **H8/14** allows some in-plane tilt with only minimal rhombic cell deformation, reducing the required out of plane tilt in the temperature range of the $Col_{rec}{}^T/p2mm^L$ phase, *i.e.* both modes of tilt are combined, though the out of plane tilt is dominating. At a certain critical temperature, however, the out-of-plane tilt wins over the in-plane tilt and strong tilt develops in the $Col_{squ}{}^T/p4mm^L$ phase with square cells (Fig. S11b and S12, ESI†). The slight rhombic deformation of the cells is obviously favored by the reduced side-chain volume compared to **H8/16**.

2.4 Reduction of R_F side chain length – angular square deformation

The in-plane tilt becomes more evident upon further side-chain shrinkage. For compound **H7/14** in addition to the alkyl chain shortening also the length (and volume) of the two R_F branches is reduced by one CF_2 group in each branch (Table 1). For this compound an optical uniaxial LC phase with spherulitic texture develops on cooling at 188 °C which in this case does not decrease, but slightly increases in birefringence down to ~140 °C (Fig. S2a–d, ESI†). The SAXS pattern in this temperature range is again indexed to a square lattice, but in this case with *p4gm* plane group and a_{squ} = 8.07–8.21 nm (Fig. 5(a)). The reconstructed ED maps show a periodic tessellation by square and rhombic cells with a rhombic angle around 52° ($Col_{squ}/p4gm$ phase, Fig. 5(b)). The larger squares contain the high ED R_F chains while the rhombic cells are filled by the low ED alkyl chains, also in this case with core–shell structure. The in-plane tilt with deformation of the squares to rhombs is obviously supported by the reduced total chain volume, favoring the formation of the smaller (rhombic) cells and the volume difference between the R_H and R_F side-chains, supporting the development of different – larger and smaller – cells. It appears that the reduction of the total chain volume is the dominating effect, because the rhombic cells are formed despite the fact that at the transition **H8/14** to **H7/14** the chain volume difference between R_F and R_H side-chains is reduced. Nevertheless, the slightly larger (5%) R_F-chain volume is obviously sufficient to select the larger square cells for the R_F-chains.

It is worth noting that the *p4gm* phase reported here is the first one combining squares and rhombs[58] in a dihedral tiling pattern, instead of the usually observed combination of squares and pairs of triangles.[49,76,84,85] This is evident from the ED maps showing the lowest ED in the middle of the rhombs (Fig. 5(b)). If there would be additional OPE cores dividing the rhombic cells into two triangles, there should be medium electron density in the middle of the rhombs. Moreover, if there would be an additional wall separating the rhombs into two triangles the triangular cells would become overcrowded as the chains of the additional molecules must be accommodated in the smaller triangular cells (see Fig. S14, ESI†).

It is remarkable that in contrast to the $Col_{squ}/p4mm^L$ phases the lattice parameter of the $Col_{squ}/p4gm$ phase increases quite a bit from a_{squ} = 8.06 nm to a = 8.23 nm upon lowering the temperature from 174 °C to 137 °C (Table 1 and inset in Fig. 5(e)). This is in line with the increase of the birefringence upon cooling in this temperature range (birefringence color changes from bluish green to yellowish green, see Fig. S2a–d, ESI†). Both effects are attributed to an increasing order parameter of the OPE rods with lowering temperature. The distance between the nodes in this tiling pattern increases from 4.2 to almost 4.4 nm on cooling, corresponding to the fully stretched molecular length. This is surprising, because in the square honeycombs (*p4mm* and $p4mm^L$) the longest achievable side length is only 3.9–4.0 nm. Moreover, changing the distance from 4.2 to 4.4 nm would simultaneously change the small inner rhombic angle between 43 and 52° (see Fig. S13a and b, ESI†), thus becoming too small at higher temperature. In fact, no change of the rhombic angle can be indicated in the ED maps where this angle remains fixed to 52° at all temperatures and for the *p4gm* phases of all compounds (see ED maps in Fig. S12, ESI†). This can be explained by a structure where the OPE cores of the molecules are shifted a bit towards the inside of the square cells (Fig. 5(d)), as previously observed for a columnar liquid quasicrystal.[30] This would require an elliptic deformation of the polar glycerol columns. To confirm the molecular packing in the *p4gm* phase, small angle neutron scattering (SANS) was conducted and the scattering length density is reconstructed in Fig. 5(c) and (d). Unlike ED maps, in which the ED sequence of different components is R_F > glycerols ≅ OPE > R_H, neutron scattering depends on the density of hydrogen atoms. Thus, the scattering density of the glycerols becomes lower than the OPE core and the sequence

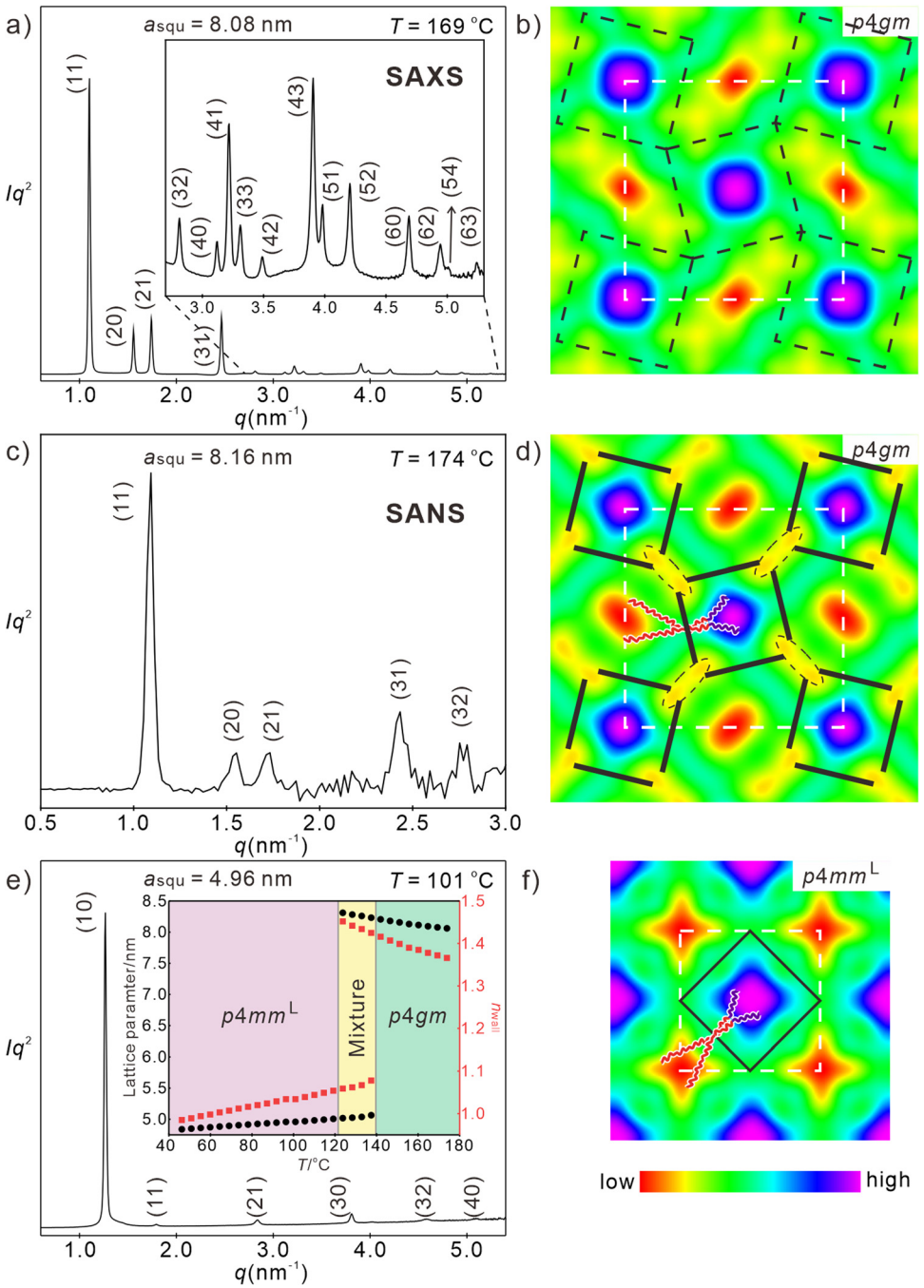

Fig. 5 Investigation of **H7/14**. (a) and (b) SAXS pattern (for numerical data, see Table S3, ESI†) and reconstructed ED map of the Col_{squ}/*p4gm* phase at 169 °C (00π0 for the first four peaks), lattice is shown by white dashed line, tiles are in black dashed lines, (c) and (d) SANS pattern (for numerical data, see Table S20, ESI†) and scattering length density of the Col_{squ}/*p4gm* phase at 174 °C (phase combination as 00000), lattice is shown by white dashed lines, glycerol nodes are shown by black dashed ellipses, tiles with molecules along edges are in black solid lines, (e) and (f) SAXS pattern (for numerical data, see Table S4, ESI†) and reconstructed ED map of the Col_{squ}/*p4mm*^{L} phase at 101 °C (0000ππ); lattice is shown by white dashed lines, tiles with molecules along edges are in black solid lines, the inset in (c) shows the temperature dependence of a_{squ} (black) and n_{wall} (red); for WAXS data, see Fig. S9a and Table S1 (ESI†), for POM textures Fig. S2 (ESI†) and for DSCs, see Fig. S1a, (ESI†).

becomes R_F > OPE > glycerols > R_H (Table S21, ESI†). The dashed ellipses in Fig. 5(d) highlight the edges of the deformed yellow hydrogen bonding columns. This deformation allows a shift of the OPE cores, leading to a shrinkage of the square side length, thus allowing an effective length of only 3.9–4.0 nm (see Fig. 5(d)) the same length as typically found in the *p4mm* phases. The shrinkage of the square cells and the simultaneous expansion of the rhombic cells reduces the volume difference between square and rhombic prismatic cells (remember, there is only 5% volume difference between R_H and R_F chains). In

this structure the centers of the square cells can more easily be reached and filled by the shorter fluorinated chains of **H7/14**, in line with the absence of blue dots with reduced ED in the centers of the R_F column (compare Fig. 3(b), (d) and 5(b), (f)). The elliptical glycerol column deformation is also associated with an increase of the wall diameter becoming 1.4 molecules on average, compared to only 1.0 in the square honeycombs (see Table 1). The additional molecules in the thicker walls fill some of the space in the rhombic cells, adjusting it to that actually required by the R_H chains.

Below a certain limiting temperature, the rhomb-square tessellation of the *p4gm* phase becomes unstable, then all angles become 90° and a transition to a square honeycomb (Fig. S1a, ESI†) with *p4mm* plane group and a_{squ} = 5.06 nm is observed at 137 °C, in line with a transition to a square chessboard tiling (see Fig. 5(e) and (f)). This transition is associated with a significant DSC peak (ΔH = 3.9 kJ mol^{-1}, Table 1 and Fig. S1a, ESI†), a reduction of n_{wall} from 1.4 to 1.0 and a strong decrease of birefringence with an inversion of birefringence at 116 °C (see Fig. S2c–e, ESI†), being the highest inversion temperature in the series **H*m*/*n***. This is in line with the strongest tilt in this $Col_{squ}{}^{T}/p4mm^{L}$ phase and the smallest a_{squ} value reaching a_{squ} = 4.83 nm (corresponding to L_{wall} = 3.4 mm and β = 39.4°) at 45 °C for this compound with the smallest side-chain volume (inset in Fig. 5(e)). Due to the significant molecular reorganization the $Col_{squ}/p4gm$ – $Col_{squ}{}^{T}/p4mm^{L}$ transition is not fully reversible but associated with a significant hysteresis, thus taking place at 137 °C on cooling and at 151 °C on heating (Table 1, for DSC, see Fig. S1a, ESI†). The WAXS remains diffuse, confirming that a fluid LC state is retained at the transition from in-plane to out-of-plane tilt. It appears that the in-plane tilt, retaining a non-tilted rod organization in the walls is entropically favored at higher temperature (reduced orientational order parameter). However, the out-of-plane tilt allows development of even smaller prismatic cells with minimized steric frustration of side chain packing by removing the tight vertices of the rhombs. Moreover, it allows a denser packing of OPE cores and chains, in line with the shift of the WAXS maximum from 0.53 at 170 °C to 0.51 nm at 50 °C (Fig. S9a and Table S1, ESI†), presumably driving this transition.

2.5 Compounds F*m*/*n* with a peripherally fluorinated FOPE core – transition from square to rectangular cells

Perfluorination of the outer benzene rings of the OPE core leads to a reduction of the LC-iso transition temperatures by 5–15 K (see Table 1). This can be attributed to (i) the larger fluorine atoms, to some extend distorting the parallel rod-alignment and hindering the hydrogen bonding networks of the adjacent glycerols, and (ii) the changing degree of incompatibility between the fluorinated cores and the R_H and R_F chains, respectively. In the series of compounds **F*m*/*n*** the $p4mm^{L}$ phase is found only for compound **F8/16**, having the longest side-chains, in a small temperature range (Fig. 6(a), (c) and (d)), while for **F8/14** it coexists in a certain temperature range with the *p4gm* phase and it has disappeared and is completely replaced by the *p4gm* phase for **F7/14** with the smallest side-chain volume (see Table 1). So, the development of the high temperature phase from $p4mm^{L}$ to *p4gm* with decreasing chain volume is the same as found for the series **H*m*/*n***, only shifted a bit towards larger total side-chain volume. The lattice parameter of the $p4mm^{L}$ phase of **F8/16** (a_{squ} = 5.5–5.6 nm, Fig. 6(a) and (b)) is very similar to that found for **H8/16**, being in line with a two-color chessboard structure and a non-tilted organization of the molecules in the honeycomb walls (L_{wall} = 4.0 nm) with approximately the same orientational order parameter as compounds **H*m*/*n***.

The *p4gm* phases of **F8/14** and **F7/14** have almost the same lattice parameters (a_{squ} = 8.1–8.2 nm) as found for **H7/14**. The ED maps (Fig. S12, ESI†) confirm that also for these compounds the high ED R_F chains (blue) fill the squares, while the low ED alkyl chains (red) are in the cores of the rhombic prismatic cells. The inner rhombic angles have the same typical value of 52°.

However, the thermal range of the mesophases without out-of-plane tilt ($p4mm^{L}$ and *p4gm*) is relatively small for all three compounds **F*m*/*n*** (3–4 K, see Table 1 and Fig. 6(a), Fig. S1b, c, ESI†) and a biaxial mesophase becomes the dominating LC phase at lower temperature. That the LC state is retained in this biaxial phase is supported by the diffuse WAXS (Fig. 6(b) and Fig. S9d–f, ESI†), supported by the WAXS (Fig. 6(b) and Fig. S9d–f, ESI†). The SAXS pattern of the biaxial low temperature phase of **F8/16** is indexed to a rectangular columnar phase with *c2mm* plane group and parameters a_{rec} = 8.32 nm and b_{rec} = 6.77 nm at 147 °C (Fig. 6(e)). The reconstructed ED map in Fig. 6(f) shows a two-color tiling by two types of rectangular instead of square tiles, *i.e.* a chessboard tiling being compressed along direction *b*. At 191 °C the transition from the $p4mm^{L}$ to the *c2mm* phase is indicated in the DSC traces of **F8/16** by a transition enthalpy of around 4 kJ mol^{-1} (Fig. 6(a)) and optically it is indicated by the emergence of significant birefringence in the homeotropic regions of the texture (insets in Fig. 6(c) and (e)). Areas with spherulite-like texture show a decrease of the birefringence, due to the onset of a tilt (see Fig. S7, ESI†). On further cooling the birefringence continuously decreases, but a relatively large negative birefringence is retained down to 40 °C without inversion of birefringence (Fig. S7, ESI†). This means the tendency to assume a tilted arrangement in the honeycomb walls is reduced for the fluorinated FOPE cores. Probably the aromatic fluorines contribute to the space filling in the prismatic cells and thus reduce the space available for the side chains and the tilt required to adjust the cell size is also reduced.

The formation of rectangular cells with only two opposite cell walls being tilted, while the others have no uniform tilt ($Col_{rec}{}^{T/2}/c2mm$, where T/2 indicates tilt of half of the walls) is unexpected. It appears that the FOPE cores cannot assume any arbitrary tilt angle, but there are two preferred modes of organization. Either without tilt which is favored by the face-to-face stacking of the electron deficit fluorinated rings on top of each other (Fig. S16b, ESI†) or a tilt around ~35–50° which is supported by the stacking interactions between the fluorinated benzenes and the electron rich triple bonds of adjacent molecules (Figs. S16d and S17, ESI†). The latter leads

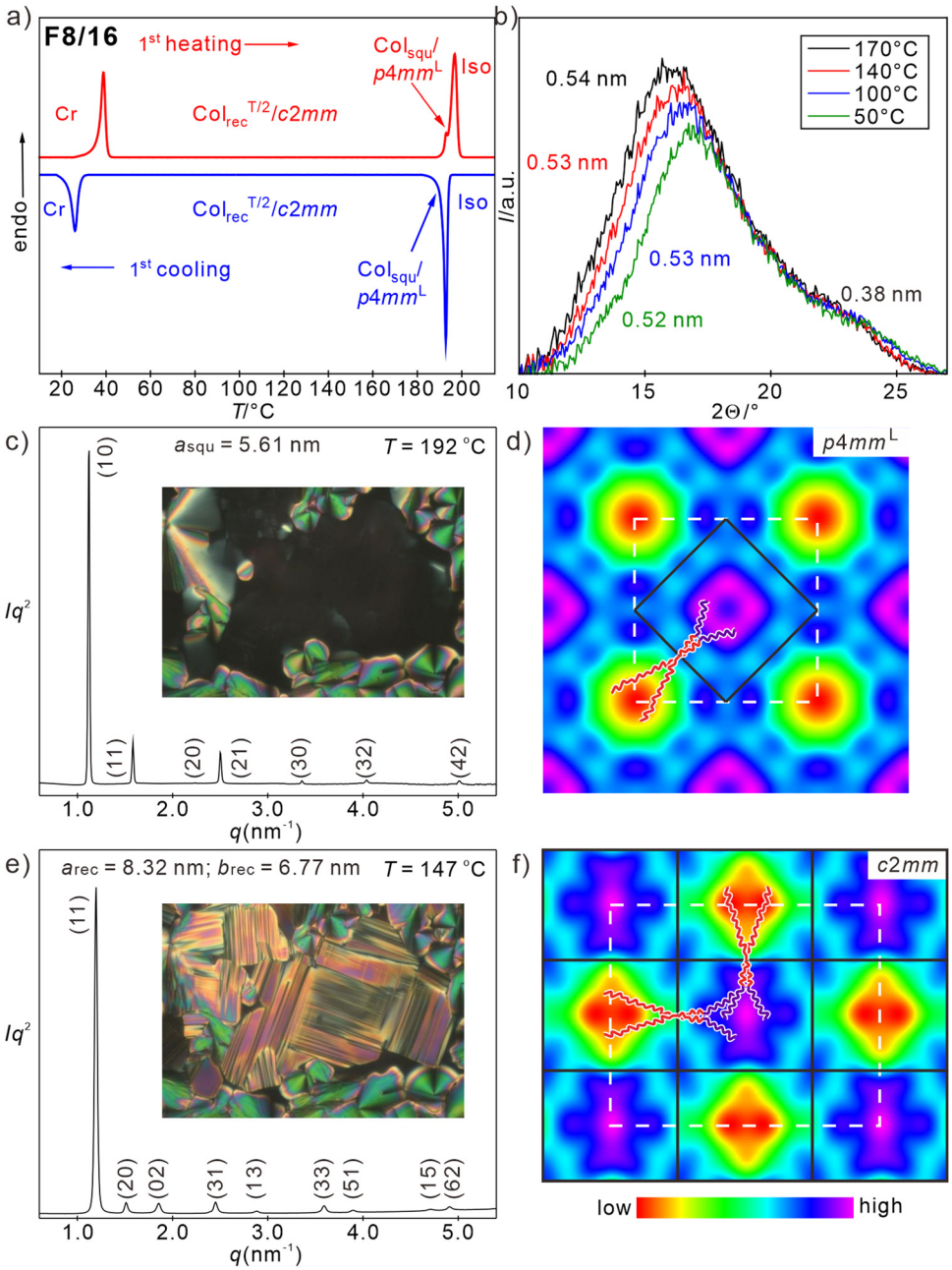

Fig. 6 Investigation of **F8/16**. (a) DSC traces and (b) WAXS patterns; (c) and (e) SAXS pattern (for numerical data, see Tables S16 and S17, ESI†) and POM textures insets (see also Fig. S7, ESI†); (d) and (f) reconstructed ED maps of (c) and (d) the $Col_{squ}/p4mm^{L}$ phase at 192 °C (0π0πππ, except for (20)) and (e) and (f) the $Col_{rec}^{T/2}/c2mm$ phase (0ππ0π00, except for (22), (13), (51) and (71)) at 147 °C; the ED of the perfluorinated benzenes contributes to the enhanced ED around the glycerol columns; lattice is shown by white dashed lines, tiles with molecules along edges are in black solid lines.

to a longitudinal shift of the OPE cores to each other,[66,86–90] providing a tilt of 35–50° if the shift takes place with uniform direction. However, increasing tilt distorts the segregation between glycerols and FOPE cores, which restricts the tilt to 30–40° in most cases. The presence of face-to-face stacking between the FOPE cores is indicated by the presence of a WAXS shoulder with a maximum corresponding to a stacking distance of d = 0.38 nm (Fig. 6(b)). However, this scattering is very diffuse, indicating only a short-range correlation of this stacking periodicity. The change of the preferred mode of core packing of compounds **F*m*/*n*** compared to compounds **H*m*/*n***, thus explains the differences between their mesophase structures and their phase sequences. In the perspective of the temperature dependence of the lattice parameters, for **F8/16**, the longer sides along direction a correspond almost to the full molecular length ($a_{rec}/2$ ~ 4.0–4.2 nm, Fig. S19a, ESI† red). The remaining two sides are significantly shorter ($b_{rec}/2$ = 3.4–3.6, Fig. S19a, ESI† red), requiring a significant tilt of about 38°. Because only 1/2 of the walls becomes significantly tilted, the average tilt over the whole structure is smaller than the Δn inversion angle of 35.3° and

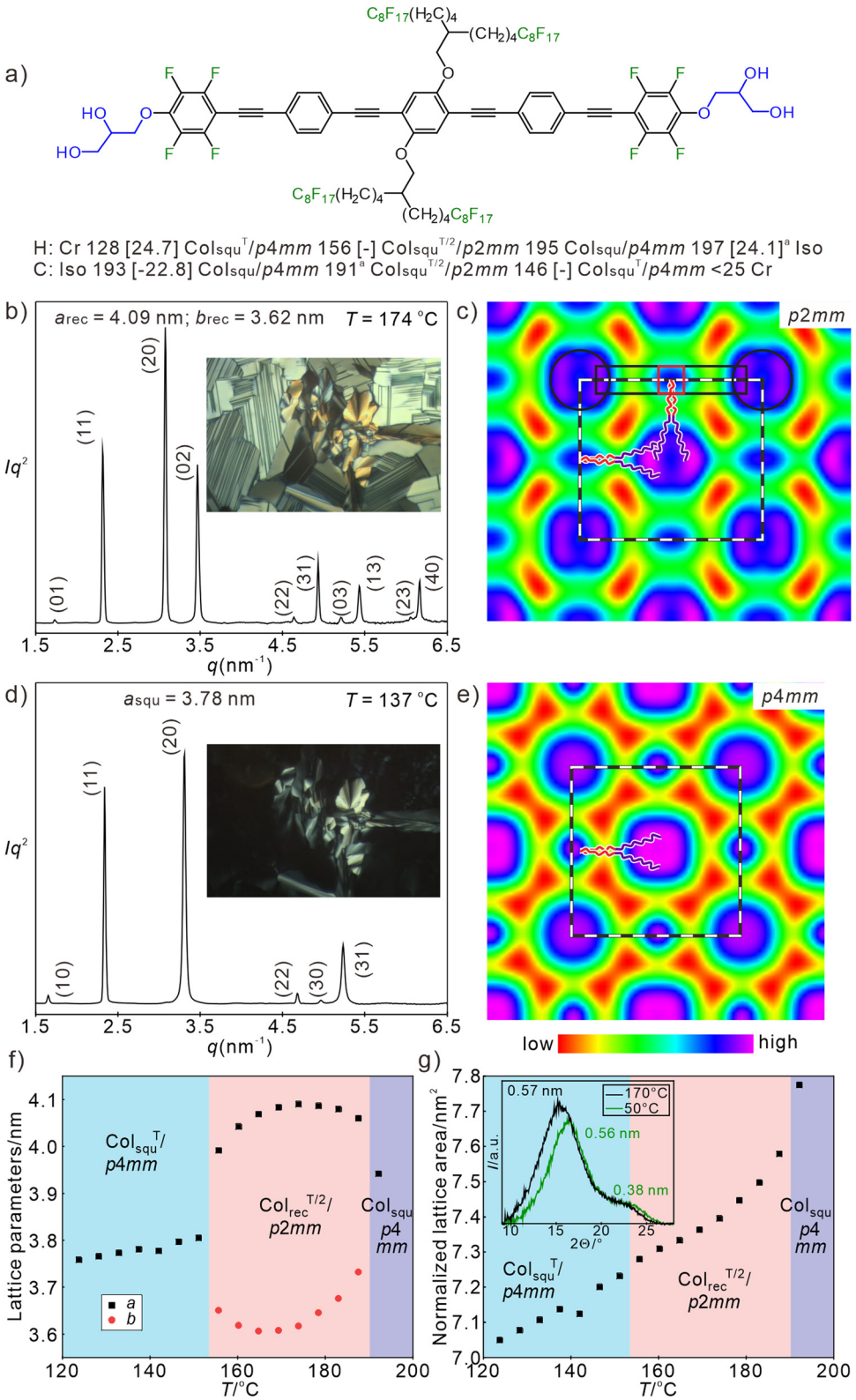

Fig. 7 Data of compound **F8$_2$**. (a) Formula and transition temperatures, (b) and (d) SAXS patterns at the indicated temperatures (for numerical data, see Tables S18 and S19, ESI†) and in the insets typical POM textures of (b) the Col$_{rec}$ $^{T/2}$/*p2mm* phase and (d) the low temperature Col$_{squ}$^{T}/*p4mm* phase. (c) and (e) ED maps reconstructed from *p2mm* pattern (phase choice: 0000ππ0ππ0) and *p4mm* pattern (phase choice: 0000ππ), dashed lines indicate the unit cell as well as one honeycomb cell, in (c) the position of one molecule is drawn, black rectangle indicates the aromatic core, red rectangle the central benzene ring and the black circles indicate the glycerol nodes; (f) and (g) temperature dependence of (f) lattice parameter and (g) normalized lattice area upon second heating and WAXS diffractograms at high (170 °C) and low temperatures (50 °C). [a]The high temperature Col$_{squ}$/*p4mm* is formed only in a very small temperature range (see Fig. S11c–e, ESI†) and immediately transforms into Col$_{rec}$$^{T/2}$/*p2mm*, the enthalpy value for both transitions cannot be separated; for WAXS pattern, see Fig. S10b and Table S1 (ESI†).

in line with the fact that for these compounds no inversion of the birefringence can be observed (Fig. S7, ESI†). Details of the development of order parameter and tilt in the distinct sides of compounds **Fm/*n*** are described in Section S2.2.7 and Fig. S19 of the ESI.†

Though tessellations by rectangular prismatic cells have previously been found in *p2mm* phases occurring below the *p4mm* square honeycombs,[91] in all previously reported cases these were single color tilings and the lattice deformation was due to an elliptical deformation of the hydrogen bonding columns at the junctions along one direction and not to an emerging tilt.[91]

For **F7/14** with the smallest side-chain volume there is an additional birefringent mesophase with mosaic-like texture and unknown structure (M1) coexisting and competing with the *p4gm* and *c2mm* phases in the temperature range between the LC-Iso transition and 140 °C (see Fig. S5, ESI†). However, the structure of this mesophase has not been resolved yet, because it cannot be obtained as a pure phase.

2.6 Compound F8$_2$ with two fluorinated side-chains at the peripherally fluorinated FOPE core – square and rectangular honeycombs with inverted sequence

Finally, let's consider the FOPE compound **F8$_2$** with two identical fluorinated side chains (Fig. 7(a)). Upon cooling it forms a tiny Col$_{squ}$/*p4mm* phase region (single color square honeycomb) of 1–2 K (a_{squ} = 3.94 nm, see Fig. S11c, ESI†), which immediately transforms into a biaxial mesophase. At this transition the homeotropic areas become birefringent, forming a 90° grid pattern as typical for a transition to a rectangular honeycomb (Fig. 7(b) inset). The diffraction pattern of this biaxial mesophase was indexed to a *p2mm* lattice with the parameters a_{rec} = 4.09 and b_{rec} = 3.62 nm (Fig. 7(b)), being about half of the corresponding values of the *c2mm* phase of **F8/16**. The parameter a_{rec} corresponds to the single molecular length and b_{rec} to a single molecule tilted by 34.6°. In line with the ED map in Fig. 7(c), this Col$_{rec}^{T/2}$/*p2mm* phase can be considered as the single-color version of the Col$_{rec}^{T/2}$/*c2mm* phase, *i.e.* it is formed by rectangular cells which are in this case all filled by the R$_F$ side chains. Similar to the single color *p4mm* phase of **H8$_2$** (Fig. 2(f) and (h)), the ED map of the *p2mm* phase of **F8$_2$** shows high ED areas (blue, purple) in the middle of the cells (R$_F$-chains) at the corners (glycerols and perfluorinated benzenes) and in the middle of the FOPE cores (dialkoxy substituted middle benzene rings). The R$_F$ columns are surrounded by medium ED shells (green) and low ED areas (yellow/red, Fig. 7(c) and (e)). These low ED areas can again be understood as regions having reduced packing density due to the difficulty to fill these spaces by the R$_F$ segments (Fig. S18b, ESI†).

As shown in Fig. 7(f), on cooling to 170 °C the b_{rec} parameter decreases to 3.6 nm *i.e.* the tilt in these shorter walls increases to 35°, while the walls along the longer sides a_{rec} become slightly longer (up to 4.1 nm) due to increasing orientational order parameter. This is in line with the locking mode of FOPE organization. However, on further cooling the parameter a_{rec} decreases and b_{rec} increases until they merge at the next transition at 148 °C. At this temperature the birefringence in the homeotropic domains (columns perpendicular to the substrate surfaces) disappears, in line with a transition to a uniaxial mesophase (Fig. 7(d), inset) and in the SAXS pattern the transition to a square phase with *p4mm* lattice is observed (Fig. 7(d)). There is no DSC peak associated with this transition (see Fig. S1e, ESI†) and the lattice parameter is 3.78 nm at 137 °C, corresponding to a single-color square honeycomb with a tilt of 30.3°; the Δn inversion is reached around 30 °C. The WAXS scattering remains diffuse in the whole investigated temperature range with its maximum shifting from 0.57 to 0.54 nm on cooling, in line with an increasing packing density (see inset in Fig. 7(g), Fig. S10b, d and Table S2, ESI†), being in line with the decreasing unit cell area with lowering temperature (Fig. 7(g)). The second diffuse scattering with clear maximum at 0.38 nm confirms the pronounced face-to-face packing in all mesophases.

Overall, on cooling the *p4mm* phase of **F8$_2$** assumes a maximum tilt of 35° in half of the honeycomb walls, leading to a rectangular honeycomb with *p2mm* plane group. On further cooling thermal chain shrinkage requires the development of a stronger tilt which obviously cannot be achieved by tilting only half of the molecules and the tilt in all honeycomb walls is required to adjust the cell size. As shown in Fig. 7(f) the tilt in the shorter walls starts expanding around 170 °C which is attributed to a decreasing tilt. This expansion is compensated by a decrease of the longer side length from 4.1 to 4.0 nm, in line with decreasing orientational order parameter. Thus, the side length difference is reduced and finally their lengths merge by assuming uniform tilt of ~30° in all four walls at the transition to the square honeycomb with uniform tilt in all walls. However, as shown for compounds **Fm/*n*** (Fig. S19a, ESI†), an angle of 35° is by far not the maximal possible tilt of the FOPE based molecules. Anyhow, the absence of the alkyl chains and the formation of a single-color tiling (*p2mm*) instead of the two-color structure (*c2mm*) disfavors rectangular and favors square cells. It seems that the absence of the longer R$_H$ chains (16–18C, compared to the shorter R$_F$ side-chains with only 13–14C) favors the smaller square cells by removing the longer non-tilted walls. Moreover, the formation of rectangular cells could be supported by the parallel alignment of the R$_H$ chains in the rectangular R$_H$-filled cells of compounds **Fm/*n***.[91] The absence of this additional rectangle stabilizing effect and the preference of the square cells by the shorter R$_F$ chains leads for **F8$_2$** to the unusual observation of the re-entrance of the square lattice and a transition from a rectangular honeycomb with lower symmetry at higher temperature (Col$_{rec}^{T/2}$/*p2mm*) to a square honeycomb (Col$_{squ}^{T}$/*p4mm*) with higher symmetry at lower temperature. For the OPE based compounds **H8$_2$** and **Hm/*n*** with non-fluorinated cores there are no rectangular cells, because there is no restriction for the tilt angle and therefore the main driving force of rectangular cell formation is absent.

3. Conclusions

In total six different self-assembled LC honeycomb structures have been identified, including 4 chessboard tiling and its derivatives (see Fig. 2, 7 and 8a). Among them the single color (Col$_{squ}$/*p4mm*) and two-color square tiling (Col$_{squ}$/*p4mm*^{L}) with

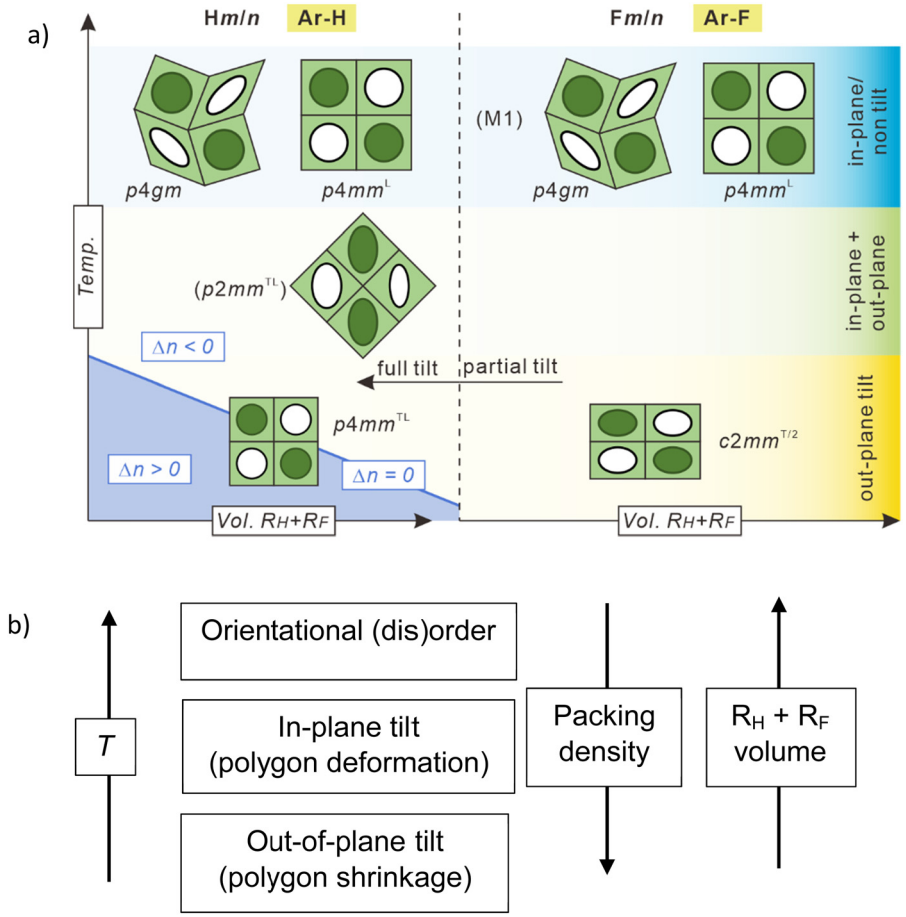

Fig. 8 (a) LC self-assembly of compounds **Hm/n** and **Fm/n** depending on side-chain volume, temperature, core-fluorination and degree of tilt of the OPE cores in the honeycomb walls. Dark green indicates domains of R_F chains, white R_H chains, and pale green areas are mixed areas; phases in parentheses are metastable or coexisting phases. (b) Development of different tilt-modes of the rod-like cores in polygonal honeycomb LC phases.

and without tilted organization of the rods in the walls and four new phases with reduced symmetry, all involving non-regular quadrangles. Three of them are derived from the chessboard (two-color square) tiling by cell deformation, namely the two-color square-rhomb tiling ($Col_{squ}/p4gm$), the three-color rhomb tiling ($Col_{rec}^{T}/p2mm^{L}$) and the stretched chessboard with rectangular cells ($Col_{rec}^{T/2}/c2mm$). The fourth one is the single-color version of the rectangular chessboard ($Col_{rec}^{T/2}/p2mm$). Remarkably, the two rectangular tessellations combine tilted and non-tilted rods in different directions of a uniform rectangular lattice.

There are two competing tilt modes, either within the crystallographic plane, leading to the deformation of square to rhombic tiles, or out of this plane, leading to cell shrinkage (Fig. 8b). Both are affected by the side-chain volume and the distinct modes of "π-stacking" interactions, tuned by aromatic core fluorination.

Packing constraints of the relatively rigid R_F segments lead to "voids" with reduced packing density in the honeycombs of the single color tilings of compounds with R_F chains at both sides and support core–shell formation with partial chain mixing in the shells for the two color tilings of compounds combining R_H and R_F side-chains.

It is also notable that in all cases the two-color tilings with segregated side chains form directly from the isotropic liquid state in a first order phase transition without an intermediate state where the side chains are still mixed, followed by an Ising transition *via* a structure with only local segregation to the long-range two-color structure, as found in all previously reported cases of chessboard tilings.[49,51] We attribute this to the pre-organization of two R_F segments in the branched side chains. This architecture also allows the use of two shorter R_F segments instead of only one with doubled length in the analogous compound with non-branched chains. This design concept is advantageous as shorter perfluorinated building blocks are more easily available and provide less solubility problems during synthesis. In addition, branched chains with shorter R_F segments have lower melting points of the crystalline phases, thus widening the LC phase ranges.

Overall, this work uncovers the importance of specific core–core interactions and space filling effects on the emergence of tilt and lattice deformation modes in multi-color quadrangular honeycomb structures achieved by soft reticular self-assembly. Modification of out-of-plane tilt by tailoring the "π-stacking" interactions is also a potential way to adjust distances between

the nodes in the related solid-state hydrogen bonded and COF-based honeycombs-like networks, especially for the creation of the still elusive quasiperiodic networks based on reticular chemistry.[72] Taking advantage of the special multicolor tiling, the rich variety of different tiling modes we found is of potential use in generating diverse soft programmable metafilm materials, which naturally requires ordered array of multi-components to interact with electromagnetic waves for light modulation and information storage. The possibility to change the birefringence from negative *via* an optically isotropic state to a positive by adjusting the tilt is of additional potential practical interest for applications in optical devices.[92]

4. Experimental

4.1 Synthesis

The synthesis (Scheme S1, ESI†) and the used procedures, together with the analytical data of all compounds are described in full detail in the ESI,† Section S3.

4.2 Investigations

Investigations were conducted by polarizing optical microscopy (POM), differential scanning calorimetry (DSC), small-angle and wide-angle X-ray scattering (SAXS and WAXS) and in one case by additional small angle neutron scattering (SANS) as described in more detail in the ESI,† Section S1.

Data availability

The data supporting this article have been included as part of the ESI.†

Conflicts of interest

There are no conflicts of interest.

Acknowledgements

This work was supported by the Deutsche Forschungsgemeinschaft (436494874 – RTG 2670), the National Natural Science Foundation of China (no 12204369), Science and Technology Agency of Shaanxi Province (2023-YBGY-459), China Postdoctoral Science Foundation (2022M712551, 2023T160505). The authors are grateful to Beamline BL16B1 at SSRF (Shanghai Synchrotron Radiation Facility, China) and BL01 at China Spallation Neutron Source (CSNS) for providing the beamtimes.

References

1 J. Uchida, B. Soberats, M. Gupta and T. Kato, *Adv. Mater.*, 2022, **34**, 2109063.
2 H. K. Bisoyi and Q. Li, *Chem. Rev.*, 2022, **122**, 4887–4926.
3 Y.-K. Kim, X. Wang, P. Mondkar, E. Bukusoglu and N. L. Abbott, *Nature*, 2018, **557**, 539–544.
4 J. Ma, J. Choi, S. Park, I. Kong, D. Kim, C. Lee, Y. Youn, M. Hwang, W. Hong and W. Kim, *Adv. Mater.*, 2023, **45**, 2302474.
5 K. Yin, E. L. Hsiang, J. Zou, Y. Li, Z. Yang, Q. Yang, P.-C. Lai, C.-L. Lin and S. T. Wu, *Light: Sci. Appl.*, 2022, **11**, 161.
6 P. J. Collings and J. W. Goodby, *Introduction to Liquid Crystals: Chemistry and Physics*, CRC Press, Boca Raton, FL, 2nd edn, 2019.
7 *Handbook of Liquid Crystals*, ed. J. W. Goodby, J. P. Collings, T. Kato, C. Tschierske, H. F. Gleeson and P. Raynes, Wiley-VCH, Weinheim, 2nd edn, 2014.
8 E.-K. Fleischmann and R. Zentel, *Angew. Chem., Int. Ed.*, 2013, **52**, 8810–8827.
9 S. Sergeyev, W. Pisula and Y. H. Geerts, *Chem. Soc. Rev.*, 2007, **36**, 1902–1929.
10 C. Tschierske, *J. Mater. Chem.*, 1998, **8**, 1485–1508.
11 C. Tschierske, *Angew. Chem., Int. Ed.*, 2013, **52**, 8828–8878.
12 B. M. Rosen, C. J. Wilson, D. A. Wilson, M. Peterca, M. R. Imam and V. Percec, *Chem. Rev.*, 2009, **109**, 6275–6540.
13 C. Tschierske and C. Dressel, *Symmetry*, 2020, **12**, 1098.
14 G. T. Stewart, *Liq. Cryst.*, 2004, **31**, 443–471.
15 D. Deamer, *Chem. Soc. Rev.*, 2012, **41**, 5375–5379.
16 H. Ringsdorf, B. Schlarb and J. Venzmer, *Angew. Chem., Int. Ed. Engl.*, 1988, **27**, 113–158.
17 F. Kuschel, A. Mädicke, S. Diele, H. Utschick, B. Hisgen and H. Ringsdorf, *Polym. Bull.*, 1990, **23**, 373–379.
18 U. Dahn, C. Erdelen, H. Ringsdorf, R. Festag, J. H. Wendorff, P. A. Heiney and N. C. Maliszewskyj, *Liq. Cryst.*, 1995, **19**, 759–764.
19 S. Diele, S. Oekiner, F. Kuschel, B. Hisgen, H. Ringsdorf and R. Zentel, *Makromol. Chem.*, 1987, **188**, 1993–2000.
20 C. Tschierske, *Chem. Soc. Rev.*, 2007, **36**, 1930–1970.
21 C. Tschierske, C. Nürnberger, H. Ebert, B. Glettner, M. Prehm, F. Liu, X.-B. Zeng and G. Ungar, *Interface Focus*, 2012, **2**, 669–680.
22 X. Cai, S. Hauche, S. Poppe, Y. Cao, L. Zhang, C. Huang, C. Tschierske and F. Liu, *J. Am. Chem. Soc.*, 2023, **145**, 1000–1010.
23 S. Poppe, A. Lehmann, M. Steimecke, M. Prehm, Y. Zhao, C. Chen, Y. Cao, F. Liu and C. Tschierske, *Giant*, 2024, 100254.
24 G. Ungar, C. Tschierske, V. Abetz, R. Holyst, M. A. Bates, F. Liu, M. Prehm, R. Kieffer, X. Zeng, M. Walker, B. Glettner and A. Zywocinski, *Adv. Funct. Mater.*, 2011, **21**, 1296–1323.
25 S. Poppe, M. Poppe, H. Ebert, M. Prehm, C. Chen, F. Liu, S. Werner, K. Bacia and C. Tschierske, *Polymers*, 2019, **7**, 471.
26 A. Scholte, S. Hauche, M. Wagner, M. Prehm, S. Poppe, C. Chen, F. Liu, X. Zeng, G. Ungar and C. Tschierske, *Chem. Commun.*, 2020, **56**, 62–65.
27 M. Poppe, C. Chen, S. Poppe, F. Liu and C. Tschierske, *Commun. Chem.*, 2020, **3**, 70.
28 F. Liu, R. Kieffer, X. Zeng, K. Pelz, M. Prehm, G. Ungar and C. Tschierske, *Nat. Commun.*, 2012, **3**, 104.
29 S. Poppe, A. Lehmann, A. Scholte, M. Prehm, X. Zeng, G. Ungar and C. Tschierske, *Nat. Commun.*, 2015, **6**, 8637.
30 X. Zeng, B. Glettner, U. Baumeister, B. Chen, G. Ungar, F. Liu and C. Tschierske, *Nat. Chem.*, 2023, **15**, 625–632.

31 Y. Cao, A. Scholte, M. Prehm, C. Anders, C. Chen, J. Song, L. Zhang, G. He, C. Tschierske and F. Liu, *Angew. Chem., Int. Ed.*, 2024, **63**, e202314454.
32 A. J. Crane, F. J. Martínez-Veracoechea, F. A. Escobedo and E. A. Müller, *Soft Matter*, 2008, **4**, 1820–1829.
33 M. Bates and M. Walker, *Soft Matter*, 2009, **5**, 346–353.
34 X. Liu, K. Yang and H. Guo, *J. Phys. Chem. B*, 2013, **117**, 9106–9120.
35 F. Liu, P. Tang, H. Zhang and Y. Yang, *Macromolecules*, 2018, **51**, 7807–7816.
36 S. D. Peroukidis, *Soft Matter*, 2012, **8**, 11062–11071.
37 M. Fayaz-Torshizi and E. A. Müller, *Mol. Syst. Des. Eng.*, 2021, **6**, 594–608.
38 Y. Sun, P. Padmanabhan, M. Misra and F. A. Escobedo, *Soft Matter*, 2017, **13**, 8542–8555.
39 T. D. Nguyen and S. C. Glotzer, *ACS Nano*, 2010, **4**, 2585–2594.
40 Z. He, X. Wang, P. Zhang, A.-C. Shi and K. Jiang, *Macromolecules*, 2024, **57**, 2154–2164.
41 Y. Sun and F. A. Escobedo, *J. Chem. Theory Comput.*, 2024, **20**, 1519–1537.
42 J. Suzuki, M. Suzuki, A. Takano and Y. Matsushita, *Macromol. Theory Simul.*, 2021, 2100015.
43 X.-Y. Yan, Q.-Y. Guo, Z. Lin, X.-Y. Liu, J. Yuan, J. Wang, H. Wang, Y. Liu, Z. Su, T. Liu, J. Huang, R. Zhang, Y. Wang, M. Huang, W. Zhang and S. Z. D. Cheng, *Angew. Chem., Int. Ed.*, 2021, **60**, 2024–2029.
44 B. Hou, W.-B. Zhang and Y. Shao, *Chin. J. Polym. Sci.*, 2023, **41**, 1508–1524.
45 S.-We Kuo, *Giant*, 2023, **15**, 100170.
46 R. Zentel, *Macromol. Chem. Phys.*, 2021, **222**, 2100216.
47 W.-Y. Chang, D. Shi, X.-Q. Jiang, J.-D. Jiang, Y. Zhao, X.-K. Ren, S. Yang and E.-Q. Chen, *Polym. Chem.*, 2020, **11**, 1454–1461.
48 X. Zeng, R. Kieffer, B. Glettner, C. Nürnberger, F. Liu, K. Pelz, M. Prehm, U. Baumeister, H. Hahn, H. Lang, G. A. Gehring, C. H. M. Weber, J. K. Hobbs, C. Tschierske and G. Ungar, *Science*, 2011, **331**, 1302–1306.
49 C. Nürnberger, H. Lu, X. Zeng, F. Liu, G. Ungar, H. Hahn, H. Lang, M. Prehm and C. Tschierske, *Chem. Commun.*, 2019, **55**, 4154–4157.
50 B. Glettner, F. Liu, X. Zeng, M. Prehm, U. Baumeister, M. A. Bates, M. Walker, P. Boesecke, G. Ungar and C. Tschierske, *Angew. Chem., Int. Ed.*, 2008, **47**, 9063–9066.
51 W. S. Fall, C. Nürnberger, X. Zeng, F. Liu, S. J. Kearney, G. A. Gehring, C. Tschierske and G. Ungar, *Mol. Syst. Des. Eng.*, 2019, **4**, 396–406.
52 M. P. Krafft and J. G. Riess, *Chem. Rev.*, 2009, **109**, 1714–1792.
53 C. Tschierske, *Top. Curr. Chem.*, 2012, **318**, 1–108.
54 L. de Campo, M. J. Moghaddam, T. Varslot, N. Kirby, R. Mittelbach, T. Sawkins and S. T. Hyde, *Chem. Mater.*, 2015, **27**, 857–866.
55 G. Johansson, V. Percec, G. Ungar and J. P. Zhou, *Macromolecules*, 1996, **29**, 646–660.
56 A. Walther and A. H. E. Müller, *Soft Matter*, 2008, **4**, 663–668.
57 M. Poppe, C. Chen, F. Liu, M. Prehm, S. Poppe and C. Tschierske, *Soft Matter*, 2017, **13**, 4676–4680.
58 A. Saeed, M. Poppe, M. B. Wagner, S. Hauche, C. Anders, Y. Cao, L. Zhang, C. Tschierske and F. Liu, *Chem. Commun.*, 2022, **58**, 7054–7057.
59 M. Poppe, C. Chen, S. Poppe, C. Kerzig, F. Liu and C. Tschierske, *Adv. Mater.*, 2020, **47**, 202005070.
60 M. Poppe, C. Chen, F. Liu, S. Poppe and C. Tschierske, *Chem. Commun.*, 2021, **57**, 6526–6529.
61 M. Poppe, C. Chen, H. Ebert, S. Poppe, M. Prehm, C. Kerzig, F. Liu and C. Tschierske, *Soft Matter*, 2017, **13**, 4381–4392.
62 M. Hird, *Chem. Soc. Rev.*, 2007, **36**, 2070–2095.
63 J. Li, H. Nishikawa, J. Kougo, J. Zhou, S. Dai, W. Tang, X. Zhao, Y. Hisai, M. Huang and S. Aya, *Sci. Adv.*, 2021, **7**, eabf5047.
64 J.-C. Liu, H. Peng, X.-G. Chen, H.-P. L, X.-J. Song, R.-G. Xiong and W.-Q. Liao, *JACS Au*, 2023, **3**, 1196–1204.
65 K. Kishikawa, *Isr. J. Chem.*, 2012, **52**, 800–808.
66 G. W. Coates, A. R. Dunn, L. M. Henling, D. A. Dougherty and R. H. Grubbs, *Angew. Chem., Int. Ed. Engl.*, 1997, **36**, 248–251.
67 M. Weck, A. R. Dunn, K. Matsumoto, G. W. Coates, E. B. Lobkovsky and R. H. Grubbs, *Angew. Chem., Int. Ed.*, 1999, **38**, 2741–2745.
68 M. Poppe, C. Chen, F. Liu, S. Poppe and C. Tschierske, *Chem. – Eur. J.*, 2017, **23**, 7196–7200.
69 C. Tang, E. M. Lennon, G. H. Fredrickson, E. J. Kramer and C. J. Hawker, *Science*, 2008, **322**, 429–432.
70 T. J. Cui, M. Q. Qi, X. Wan, J. Zhao and Q. Cheng, *Light: Sci. Appl.*, 2014, **3**, e218.
71 M. Paquay, J. C. Iriarte, I. Ederra, R. Gonzalo and P. de Maagt, *IEEE Trans. Antennas Propag.*, 2007, **55**, 3630–3638.
72 F. Haase and B. V. Lotsch, *Chem. Soc. Rev.*, 2020, **49**, 8469–8500.
73 S. B. Alahakoon, S. D. Diwakara, C. M. Thompson and R. A. Smaldone, *Chem. Soc. Rev.*, 2020, **49**, 1344–1356.
74 Y. Jin, Y. Hu and W. Zhang, *Nat. Rev. Chem.*, 2017, **1**, 0056.
75 R.-R. Liang, S.-Y. Jiang, R.-H. A and X. Zhao, *Chem. Soc. Rev.*, 2020, **49**, 3920–3951.
76 F. Haase, G. A. Craig, M. Bonneau, K. Sugimoto and S. Furukawa, *J. Am. Chem. Soc.*, 2020, **142**, 13839–13845.
77 S. E. Wheeler and K. N. Houk, *Mol. Phys.*, 2009, **107**, 749–760.
78 G. N. Patwari, P. Venuvanalingam and M. Kolaski, *Chem. Phys.*, 2013, **415**, 150–155.
79 M. Born and E. Wolf, *Principles of Optics*, Pergamon, Oxford, 1980.
80 V. Percec, A. E. Dulcey, V. S. K. Balagurusamy, Y. Miura, J. Smidrkal, M. Peterca, S. Nummelin, U. Edlund, S. D. Hudson, P. A. Heiney, H. Duan, S. N. Magonov and S. A. Vinogradov, *Nature*, 2004, **430**, 764–768.
81 M. Lehmann, M. Dechant, M. Lambov and T. Ghosh, *Acc. Chem. Res.*, 2019, **52**, 1653–1664.
82 C. Tschierske, Microsegregation in Liquid Crystalline Systems: Basic Concepts, in *Handbook of Liquid Crystals*, ed. J. W. Goodby, J. P. Collings, T. Kato, C. Tschierske, H. F. Gleeson and P. Raynes, Wiley-VCH, Weinheim, 2014, vol. 5, pp. 1–43.

83 C. Tschierske, *Isr. J. Chem.*, 2012, **52**, 935–959.
84 B. Chen, X. Zeng, U. Baumeister, G. Ungar and C. Tschierske, *Science*, 2005, **307**, 96–99.
85 X. Cheng, H. Gao, X. Tan, X. Yang, M. Prehm, H. Ebert and C. Tschierske, *Chem. Sci.*, 2013, **4**, 3317–3331.
86 J. W. Steed and J. L. Atwood, *Supramolecular Chemistry*, Wiley, Chichester, UK, 2nd edn, 2009.
87 C. A. Hunter and J. K. M. Sanders, *J. Am. Chem. Soc.*, 1990, **112**, 5525–5534.
88 S. E. Wheeler, *Acc. Chem. Res.*, 2013, **46**, 1029–1038.
89 K. Carter-Fenk and J. M. Herbert, *Phys. Chem. Chem. Phys.*, 2020, **22**, 44870–44886.
90 A. Kundu, S. Sen and G. N. Patwari, *J. Phys. Chem.*, 2020, **124**, 7470–7477.
91 A. Lehmann, A. Scholte, M. Prehm, F. Liu, X. Zeng, G. Ungar and C. Tschierske, *Adv. Funct. Mater.*, 2018, **28**, 1804162.
92 S. Lagerwall, A. Dahlgren, P. Jägemalm, P. Rudquist, K. D'have, H. Pauwels, R. Dabrowski and W. Drzewinski, *Adv. Funct. Mater.*, 2001, **11**, 87–94.